Status for the two-dimensional Navier-Stokes solver EllipSys2D

Bertagnolio, Franck; Sørensen, Niels N.; Johansen, J.

Publication date:
2001

Document Version
Publisher's PDF, also known as Version of record

Risø–R–1282(EN)

Status for the Two-Dimensional Navier-Stokes Solver EllipSys2D

Franck Bertagnolio, Niels Sørensen and
Jeppe Johansen

Risø National Laboratory, Roskilde, Denmark
August 2001

Abstract This report sets up an evaluation of the two-dimensional Navier-Stokes solver EllipSys2D in its present state. This code is used for blade aerodynamics simulations in the Aeroelastic Design group at Risø. Two airfoils are investigated by computing the flow at several angles of attack ranging from the linear to the stalled region. The computational data are compared to experimental data and numerical results from other computational codes. Several numerical aspects are studied, as mesh dependency, convective scheme, steady state versus unsteady computations, transition modelling. Some general conclusions intended to help in using this code for numerical simulations are given.

ISBN 87–550–2914–0
ISBN 87–550–2915–9(Internet)
ISSN 0106–2840

Print: Pitney Bowes Management Services Danmark A/S · 2001

Contents

1 Introduction *5*

2 DU-91-W2-250 Airfoil *6*
- 2.1 Influence of the mesh refinement *6*
- 2.2 Influence of the mesh type *7*
- 2.3 Transition to turbulence *7*
- 2.4 Influence of the convective scheme *8*
- 2.5 Comparison between steady and unsteady simulations *9*

3 A-Airfoil *21*
- 3.1 Influence of the mesh *21*
- 3.2 Influence of the convective scheme *22*
- 3.3 Comparison between steady and unsteady simulations *23*
- 3.4 Comparison with other computational codes *23*

4 Conclusions *38*

References *39*

1 Introduction

The aim of this report is to evaluate the capabilities of the numerical Navier-Stokes flow solver EllipSys2D for the computation of flowfields around airfoils. This code has been developed jointly at DTU and Risø by Michelsen and Sørensen (see [9, 10, 13] for a detailed description of the numerical code). It is designed to solve the two-dimensional Navier-Stokes equations for an incompressible fluid. It uses a cell-centered grid arrangement for the pressure field and the cartesian velocity components. The equations are discretised by means of a finite volume formulation. The well-known velocity-pressure decoupling is circumvented by using the Rhie and Chow interpolation technique [12]. The SIMPLE algorithm is used for solving the momentum and pressure equations in a predictor-corrector fashion [11].

The computational domain has to be mapped onto a boundary-fitted structured grid. In order to facilitate the mapping and to take advantage of the new generation of parallel computers, a domain decomposition technique has been implemented. The meshes of the individual subdomains must be conformal, i.e. the grid lines must match at the interfaces between the subdomains.

It must be noted that all the computational grids that are used in this report are generated with the program HypGrid2D developed by Sørensen [14]. This is a hyperbolic grid generator that is designed to create both C-type and O-type structured meshes around airfoils.

In this report, several airfoils and configurations are tested. When available, the computational results will be compared to experimental data and/or computational results from other numerical codes.

2 DU-91-W2-250 Airfoil

The airfoil that is studied in this section has a relative thickness of 25% and is dedicated to wind turbine applications. Its profile is plotted on Figure 1. It was designed at the Delft University and tested in a low-speed low-turbulence wind tunnel by Timmer and van Rooy [15]. Only the experiments conducted on an airfoil with smooth surface at a Reynolds number of 1×10^6 (based on the inflow velocity and chord length of the profile) are considered hereafter.

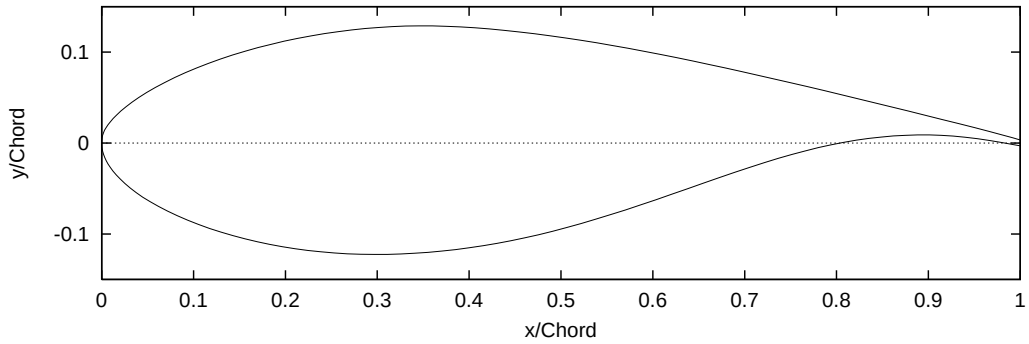

Figure 1. Shape of the DU-91-W2-250 Airfoil

The study involves the influence of the mesh and of the scheme used for the discretisation of the convective term, the comparison of steady and unsteady computations, as well as the influence of the time step for the unsteady ones.

2.1 Influence of the mesh refinement

Several computations are conducted with different meshes. The meshes that are used for all these computations with this airfoil (including in the remaining of this section, unless otherwise specified) are O-type meshes, in order to provide a better mesh resolution of its blunt trailing edge.

Four different meshes are considered. The coarsest one, herafter denoted as mesh M0, has 64 cells in the direction away from the airfoil, and 256 in the direction around the airfoil. The height of the cells adjacent to the airfoil is 1×10^{-5} chord length. The second mesh M1 is similar to M0 except that it has 384 cells around the airfoil. A third refined mesh M2 is designed by taking the mesh M1 and merely doubling the number of cells. As a consequence, cells adjacent to the airfoil are half the size of those of mesh M1. These three meshes extent 15 chords away from the airfoil. Finally, a mesh M3 is created similarly to mesh M1, except that it extents within 30 chords away from the airfoil. For doing this, it has 128 cells in the direction away from the airfoil and still 384 cells in the other direction, which means that both meshes are identical in the vicinity of the airfoil.

In this section, the SUDS-scheme with limiter, and a transition model are used for all computations (see further for tests on the convective scheme and transition model).

The lift, drag and pitching moment coefficients as functions of the angle of attack obtained for the different meshes are displayed on Figures 2, 3 and 4, respectively. In addition, the experimental data are reported. As it can be seen on these figures, the results are nearly insensitive to both the mesh refinement and the extension of the mesh. However, it must be noted that the pitching moment coefficient is a bit more sensitive to the mesh in the stalled region. This allows us to assume that

the computation are converged with respect to the mesh.

In the remaining of this section, only mesh M1 is used for all computations, unless otherwise specified.

2.2 Influence of the mesh type

Two different types of mesh are compared: a O-type and a C-type mesh. The O-mesh is identical to mesh M1 introduced in the previous section. The C-mesh is such that the cell distribution on the surface of the airfoil is identical to the one of mesh M1, the number of cell away from the airfoil being also the same as mesh M1. 64 cells are added to the C-mesh in order to extend the mesh in the airfoil's wake. Morevover, the simulations are performed using the SUDS-scheme, both with and without the limiter.

As can be seen on the lift, drag and pitching moment coefficients curves (Figures 5, 6 and 7, respectively), the influence of the mesh type is quite small.

In this second test, the mesh configuration in the wake of the airfoil is modified in an attempt to improve the results. Four meshes are compared. The first one is the O-mesh M1 used before. The second one is the C-mesh also used before for which the mesh line originating from the trailing edge was approximately parallell to the mean chord of the airfoil. A third mesh, which is designated as 'adapted', is such that this mesh lines is approximately orientated in the direction of the wake of the flow. In our case, the angle beween the mean chord of the airfoil and the wake mesh line is 10^o. It is then expected that the wake of the flow will be more accurately captured by this mesh. As some numerical instabilities occured in some computations with this last mesh, a new mesh was designed for which the cells with extreme aspect ratio in the vicinity of the wake (mesh) line were expanded in the direction perpendicular to the wake. It is named 'open' mesh in the following. Note that all C-meshes have the same number of cells and the same cell sizes around the airfoil. The SUDS scheme without limiter is used for the convective terms.

Lift and drag coefficients curves are depicted on Figs. 8, 9, respectively. As it can be seen, the influence of the mesh is relatively small. The need for an adapted open mesh is then only justified by numerical stability reasons in this case.

2.3 Transition to turbulence

As the Reynolds number considered in this test case is relatively low, transition to turbulence has to be addressed. For all computations, the $k-\omega$ SST (Shear Stress Transport) turbulence model by Menter [7] has been used.

As a first assumption, the flow can be considered as fully turbulent, i.e. the turbulent viscosity is directly given by the turbulence model that is implemented in the numerical code.

Secondly, a transition model can be introduced. Its purpose is to determine a location along the surface of the profile (according to the fulfilment of a specifically designed criterion), such that the flow can be considered as laminar upstream this point, and as transitional downstream. As a consequence, the turbulent viscosity is switched off on the boundary layer stations upstream the transition point. Downstream, the turbulent viscosity on the boundary layer stations is given by the turbulence model. However, in order to model the turbulence intermittency that occurs in transitional flows, the turbulent viscosity is weighted by a multiplicative factor that grows from 0 (at the transition point) to 1 (at the end of the transitional region) according to an empirical function given by Chen and Thyson [1]. In our case, the transition model by Michel [8] is used.

As can be seen on Figures 10 and 11, there are substantial discrepancies in the lift and drag curves obtained with a fully turbulent flow or with the Michel transition model.

Firstly, in the linear region (approximately for an angle of attack below 10^o), the fully turbulent simulations underestimate the lift, whereas the computations with transition model perfectly match the experimental data. This mismatching of the fully turbulent computation can be explained by the fact that the turbulent boundary layer develops earlier than in the real case, inducing additional skin friction in the area between the leading edge and the actual transition point, on the suction side. At the same time, the pressure on the airfoil is reduced, decreasing the computed lift. Both pressure and skin friction coefficients along the airfoil surface for an angle of attack of $\alpha = 7.686^o$ are displayed on Figures 12 and 14. As mentioned, the pressure coefficient is much closer to the experimental data with the transition model than for the fully turbulent flow. On the suction side, a small recirculation bubble starting at the relative abscisse $x/C = 0.37$ can be detected from the skin friction distribution for the computation with transition model. For the fully turbulent computation, this bubble doesn't exist, but on the other hand, a separation region occurs at the trailing edge starting at $x/C = 0.9$.

In the stalled region (well beyond 10^o), the situation is quite different. Indeed, it is now the simulations with transition that tend to overpredict the lift of the airfoil, and underpredict the drag (see Figure 10 and 11). Fully turbulent computations exhibit the same tendencies, but to a smaller extent. Not much can be said to explain these discrepancies. Indeed, for those high angles of attack, the flow is highly separated and the turbulence structures that originate from this detached area are surely three-dimensional. Thus, these 2D simulations might not be able to described the main features of the flow, and thereby fail to predict the correct forces on the airfoil.

2.4 Influence of the convective scheme

Two basic types of scheme are tested: the Second order Upwind Differencing Scheme (SUDS) [16] and the Quadratic Upstream Interpolation for Convection Kinematics (QUICK) [6]. In order to increase the stability of the numerical methods, it is common to make use of a limiter for the convective term. In our case, the 'min-mod' limiter [5] has been implemented.

These three configurations are compared, together with the experimental data, on Figures 16, 17 and 18 which represents the lift, drag and pitching moment coefficients as functions of the angle of attack, respectively. As it can be seen, in the linear region all schemes give good results in comparison with the experimental data. In the stalled region, however, they perform differently. Paying attention to the SUDS-scheme, it is clear that the limiter has an undesirable effect on the lift and pitching moment coefficients. The drag coefficient is much less sensitive.

These two statements can be recovered in the pressure coefficient distribution along the airfoil. Indeed, it can be seen that, for an angle of attack located in the stalled region (15.19^o on Fig.20), this coefficient noticeably differs for the computations with or without limiter, whereas the two curves are nearly the same for an angle of attack in the linear region (7.686^o on Fig.19).

The above mentioned figures also displayed the results obtained with the QUICK-scheme. The lift curve (Fig.16) clearly shows that this scheme has a tendency to overestimate the lift in the region intermediate between the beginning of the stall and the deep stalled region. However, the curve is getting closer to the experimental data when the airfoil enters in deep stall (approximately over 14^o). As for the drag coefficient (Fig.17), the results are quite insensitive to the scheme until the deep stall region where the QUICK-scheme seems to perform better as well. The

pitching moment coefficient gives another tendency, namely the results deteriorate in deep stall.

It must be noted that the apparent better performance of the QUICK-scheme might be a coincidence. Indeed, the results obtained with this scheme exhibit a high level of variations in the course of the steady state computation. The force coefficients are computed by averaging over several periods of oscillations for which the pseudo-transient phase of the simulation is terminated. As these simulations are performed in a steady state mode, the results do not necessarily represent the true physics of the phenomenon.

2.5 Comparison between steady and unsteady simulations

The purpose of this section is to compare the results obtained with a steady state computation and the averaged data from an unsteady computation. As for the latter one, the results presented thereafter are averaged in time. The averaging procedure is initiated when the transient phase of the simulation is terminated.

Firstly, the results of a steady state computation and an unsteady computation (with time step $\Delta t = 1 \times 10^{-2}$) are compared for the SUDS-scheme with limiter and the QUICK-scheme. Lift and drag coefficients are reported on Figures 22 and 23, respectively. It can be seen that the SUDS-scheme behaves quite similarly in a steady state mode or in an unsteady simulation. In opposite, the QUICK scheme behaves poorly for an unsteady computation.

Secondly, the influence of the time step on the unsteady computation is investigated. The SUDS-scheme with and without limiter are used. Three different time steps are considered: $\Delta t = 1 \times 10^{-2}$, 1×10^{-3} and 4×10^{-4}. Figs.24 and 25 show the lift coefficient obtained for these two schemes and for the different time steps. It can be seen that the results seem to slightly deteriorate as the time step decreases (in comparison with the experimental data) for the scheme with limiter. As for the scheme without limiter, the lift curves also evolve as the time step decreases, but with an opposite tendency (namely, the lift is decreasing, when it was increasing for the scheme with limiter). The pressure and skin friction coefficients for these different time steps, for the scheme without limiter, and for an angle of attack $\alpha = 15.19^o$, are reported on Figs.26 and 27. The main differences seem to be located in the transition area and in the region just downstream of the laminar separation bubble.

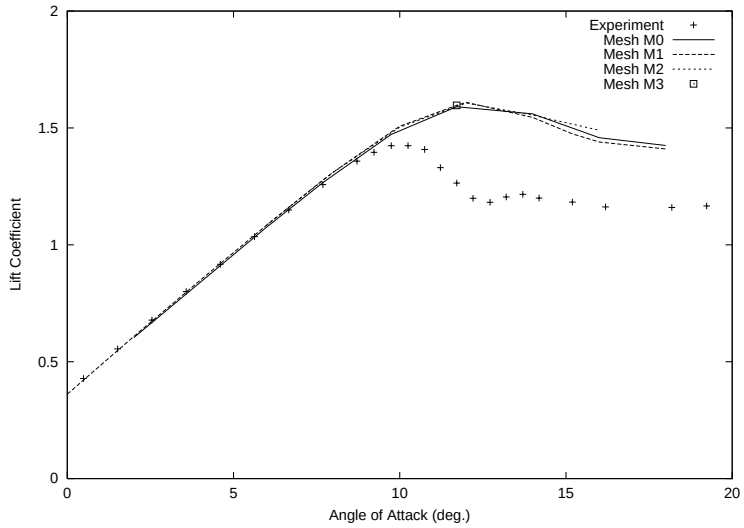

Figure 2. Lift Coefficient Curves for the Different Meshes

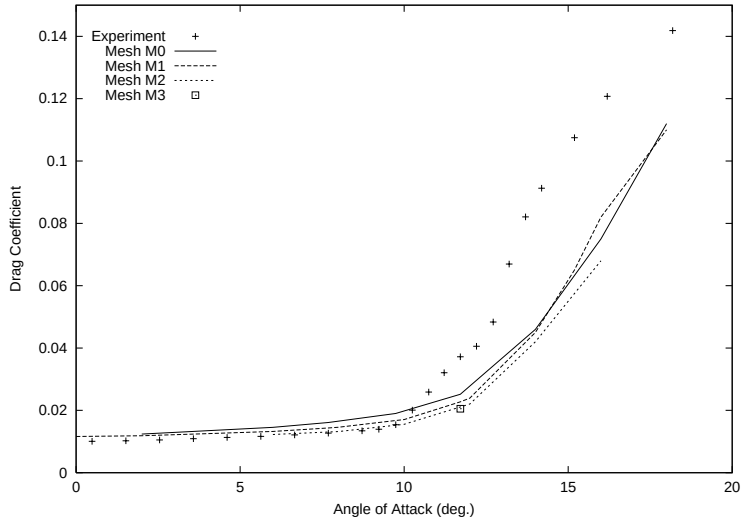

Figure 3. Drag Coefficient Curves for the Different Meshes

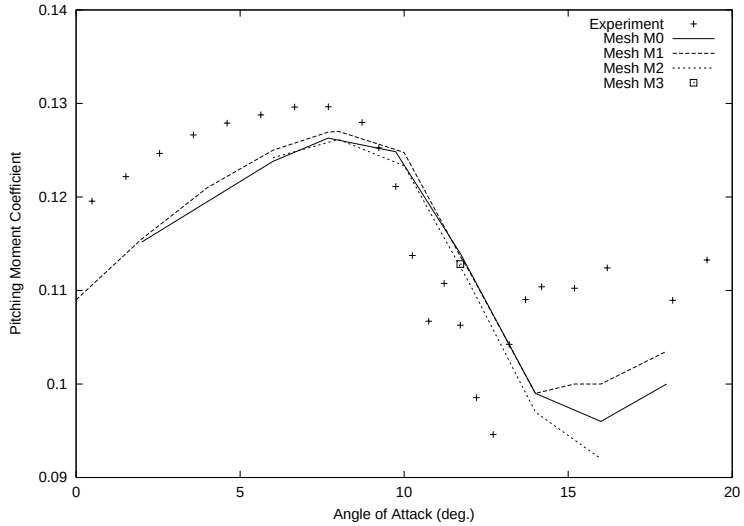

Figure 4. Pitching Moment Coefficient Curves for the Different Meshes

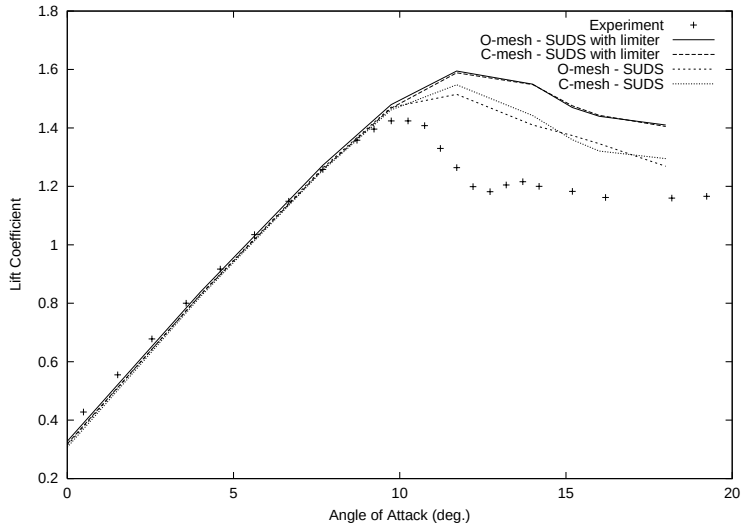

Figure 5. Lift Coefficient Curves for the O- and the C-Mesh

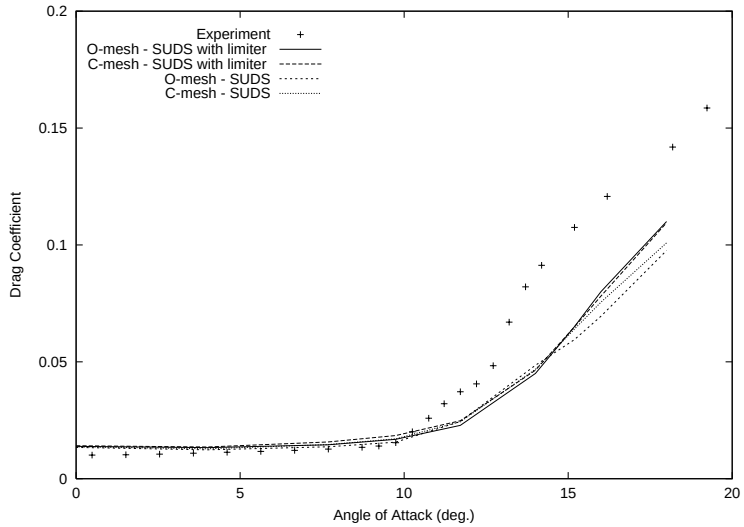

Figure 6. Drag Coefficient Curves for the O- and the C-Mesh

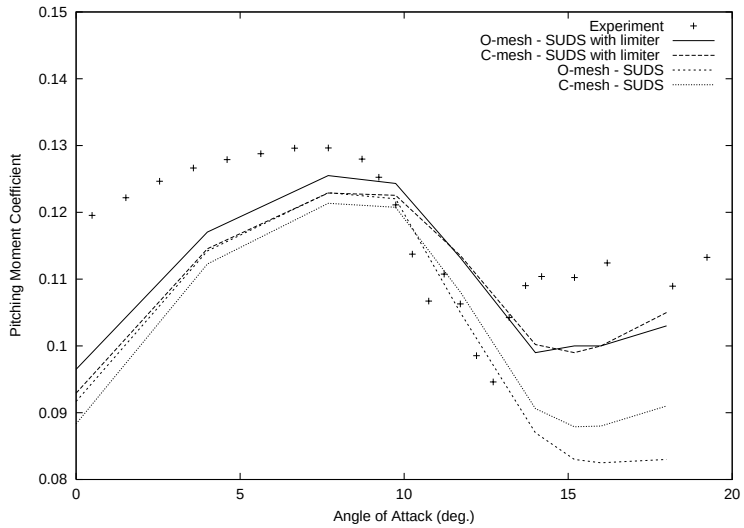

Figure 7. Pitching Moment Coefficient Curves for the O- and the C-Mesh

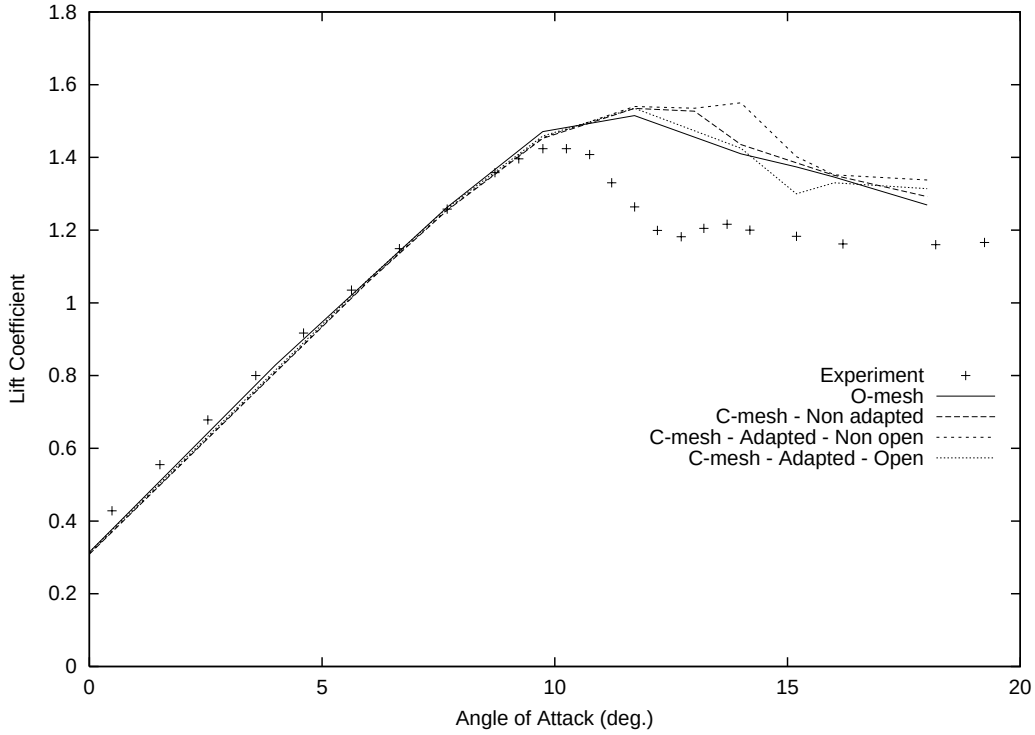

Figure 8. Lift Coefficient Curves for the O-Mesh and Several C-Meshes

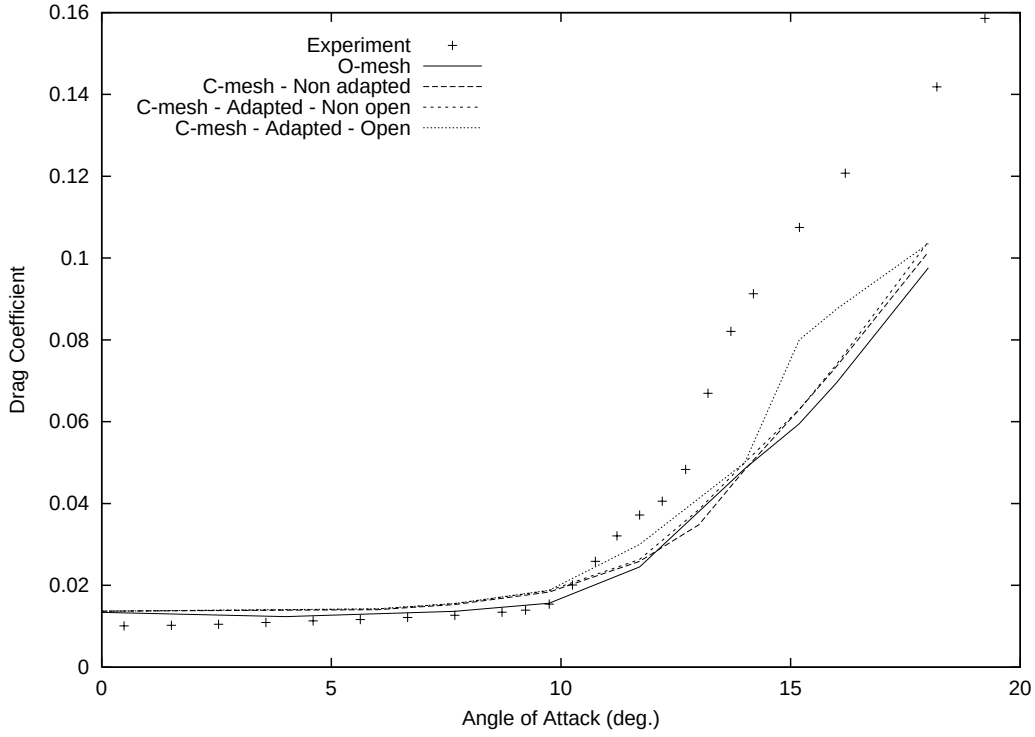

Figure 9. Drag Coefficient Curves for the O-Mesh and Several C-Meshes

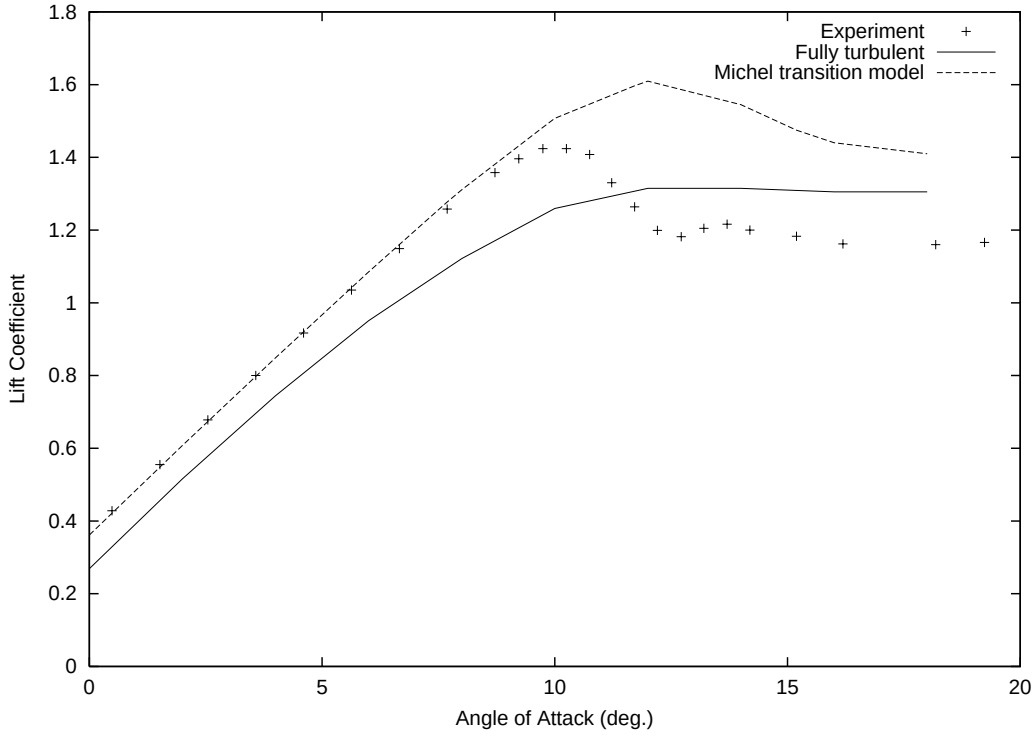

Figure 10. Lift Coefficient Curves with and without Transition Model

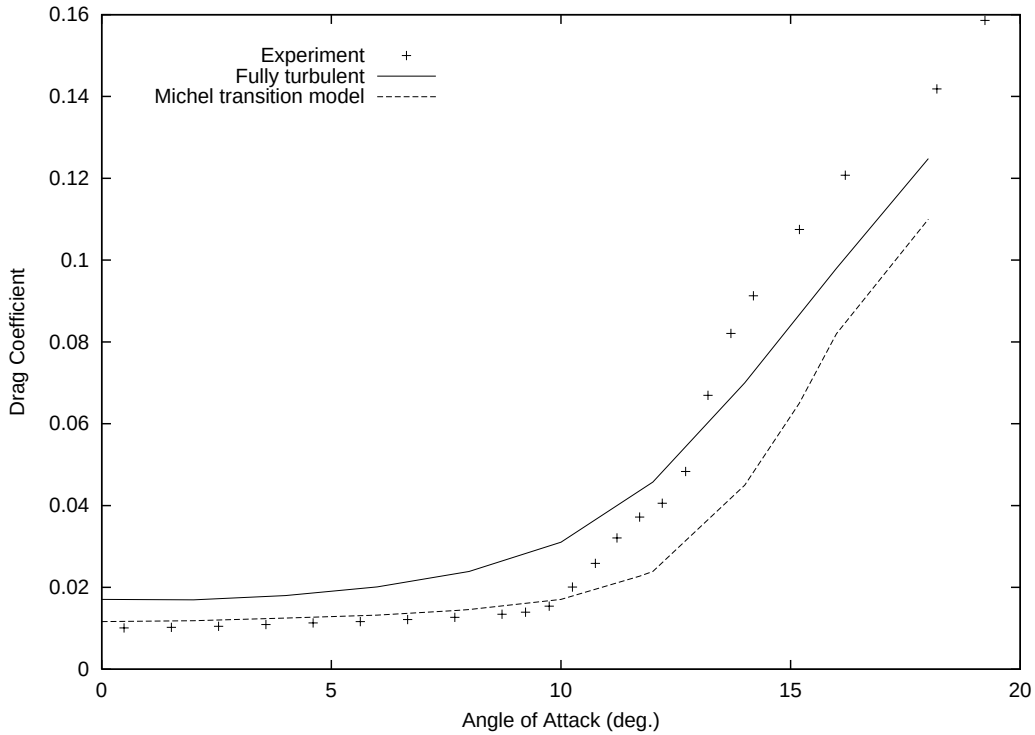

Figure 11. Drag Coefficient Curves with and without Transition Model

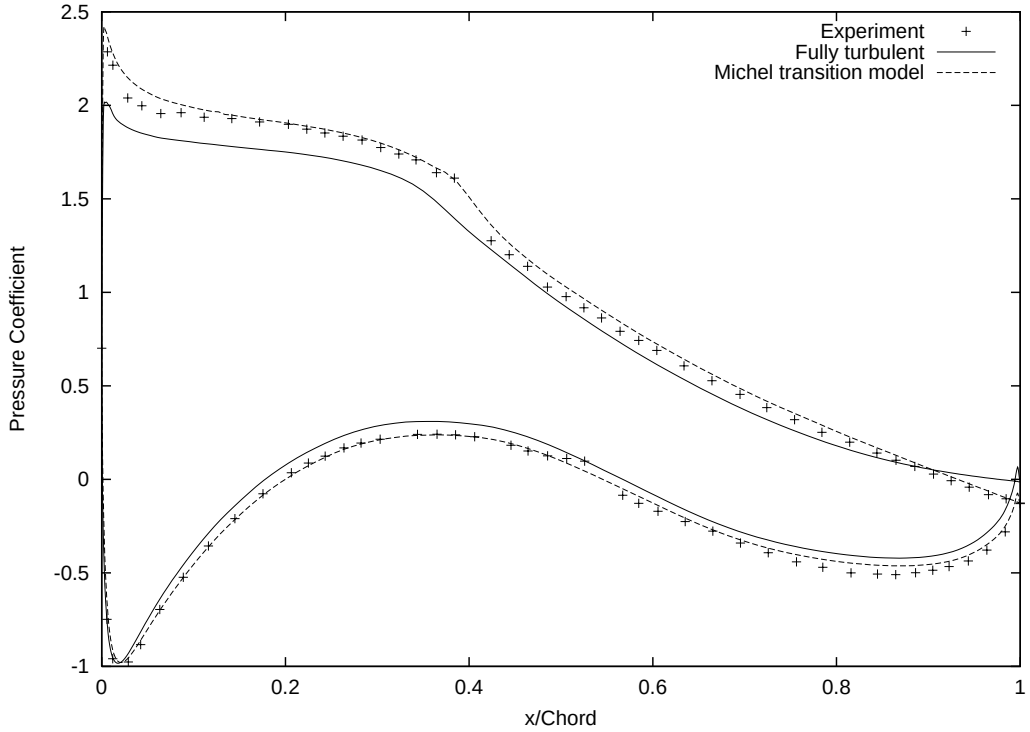

Figure 12. Pressure Distribution with and without Transition Model at $\alpha = 7.686^o$

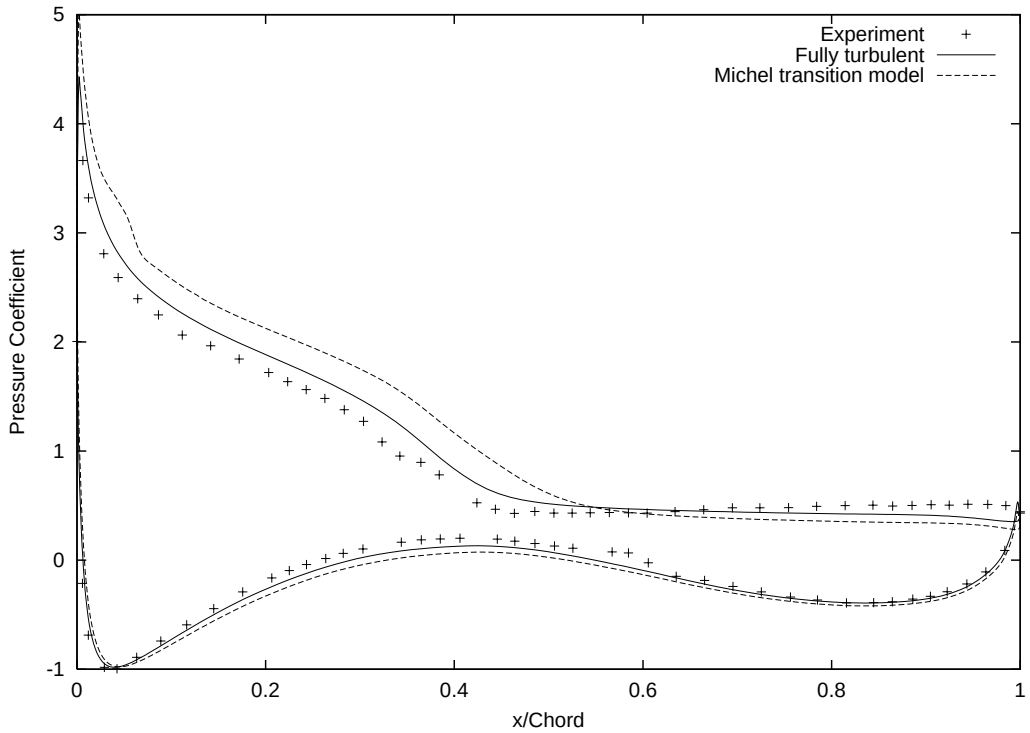

Figure 13. Pressure Distribution with and without Transition Model at $\alpha = 15.19^o$

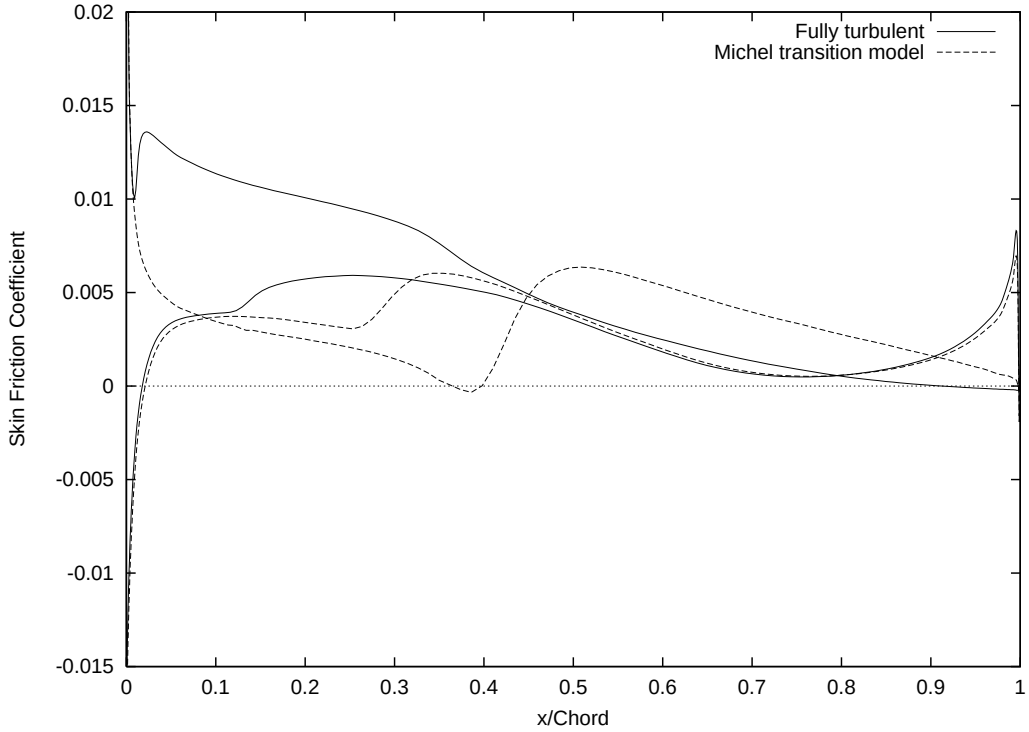

Figure 14. Skin Friction Distribution with and without Transition Model at $\alpha = 7.686^o$

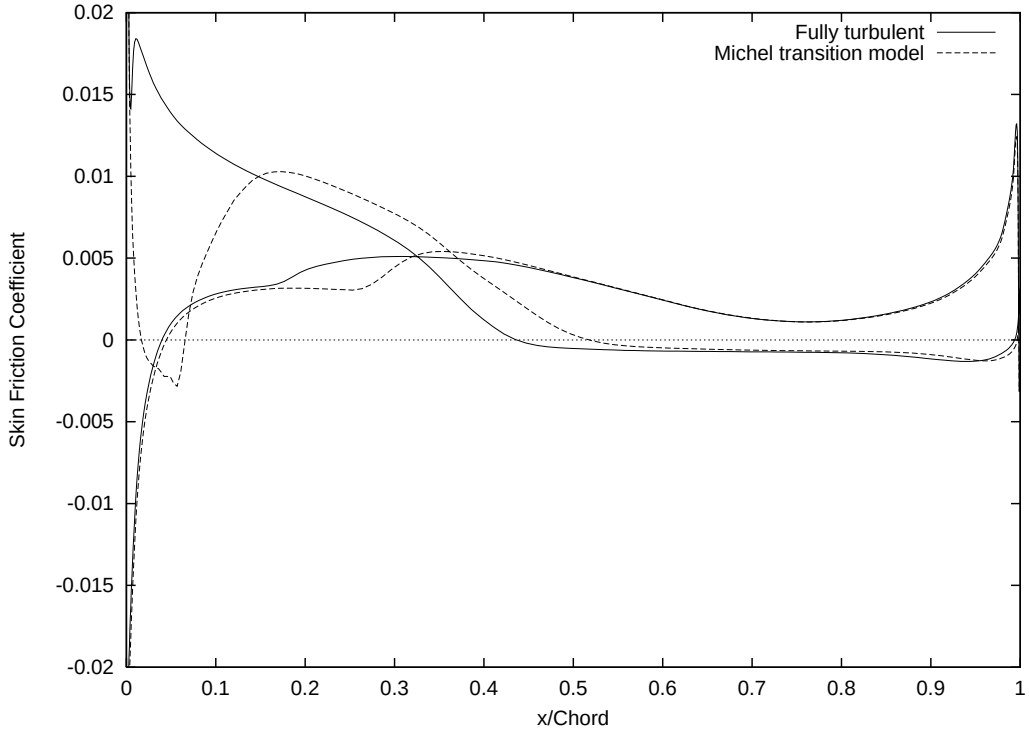

Figure 15. Skin Friction Distribution with and without Transition Model at $\alpha = 15.19^o$

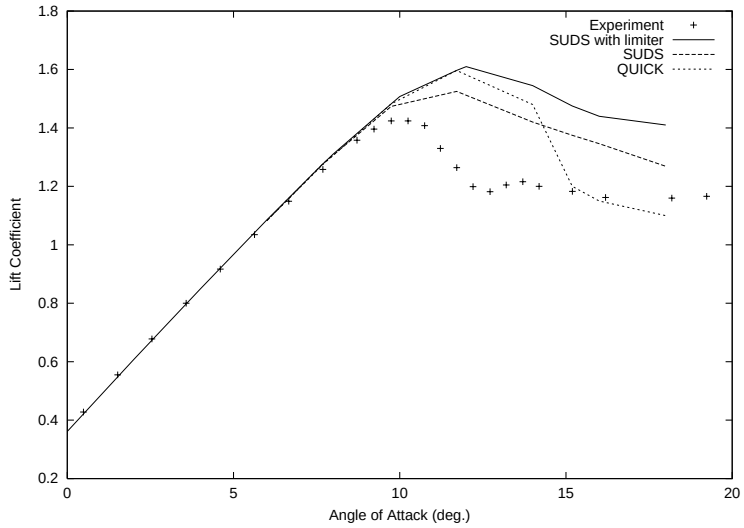

Figure 16. Lift Coefficient Curves for the Different Convective Schemes

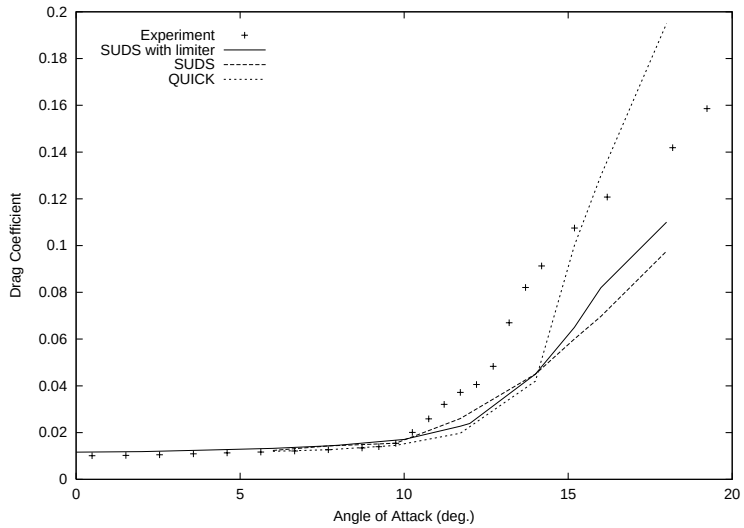

Figure 17. Drag Coefficient Curves for the Different Convective Schemes

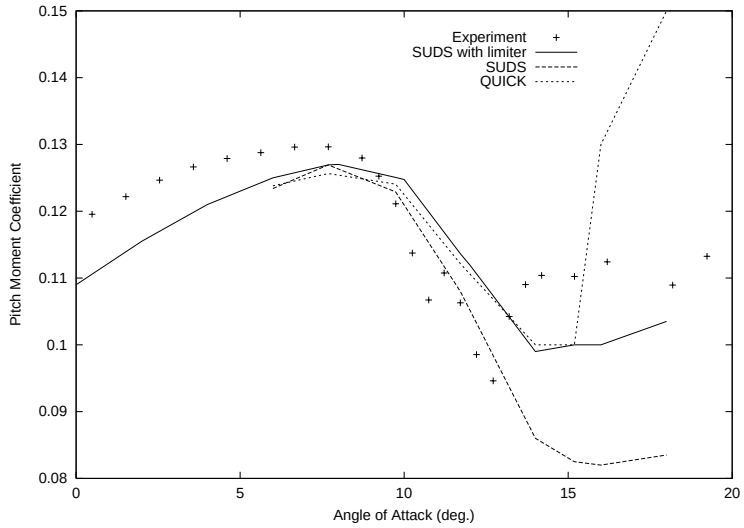

Figure 18. Pitching Moment Coefficient Curves for the Different Convective Schemes

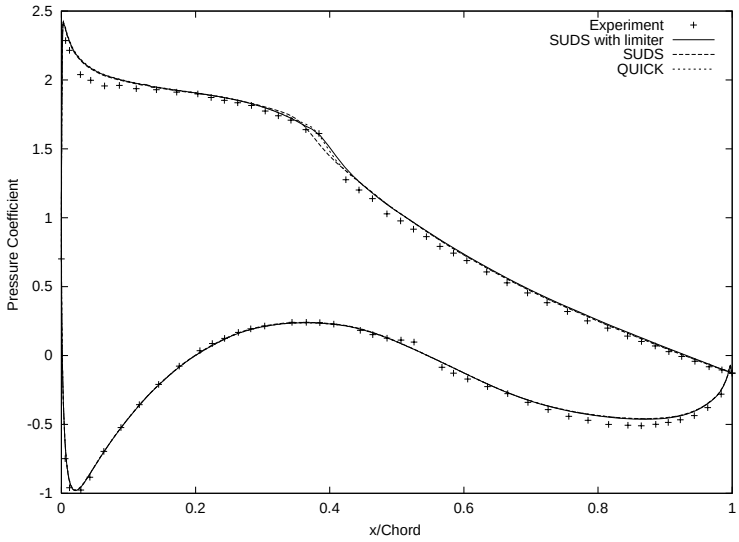

Figure 19. Pressure Distribution for the Different Convective Schemes at $\alpha = 7.686^o$

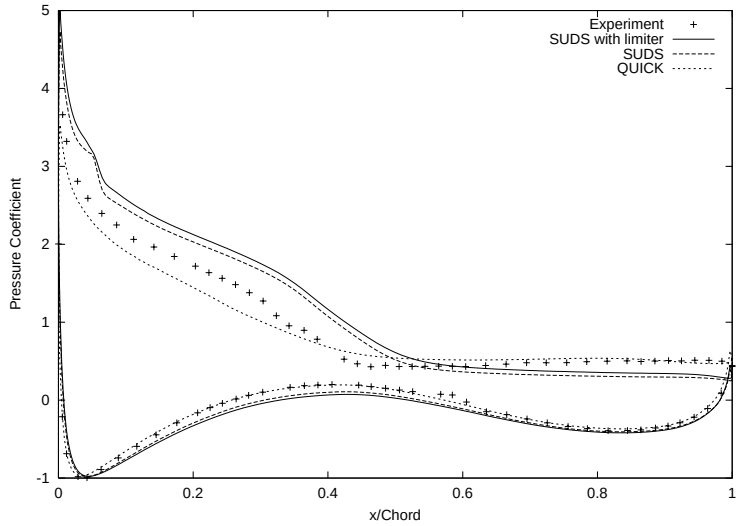

Figure 20. Pressure Distribution for the Different Convective Schemes at $\alpha = 15.19^o$

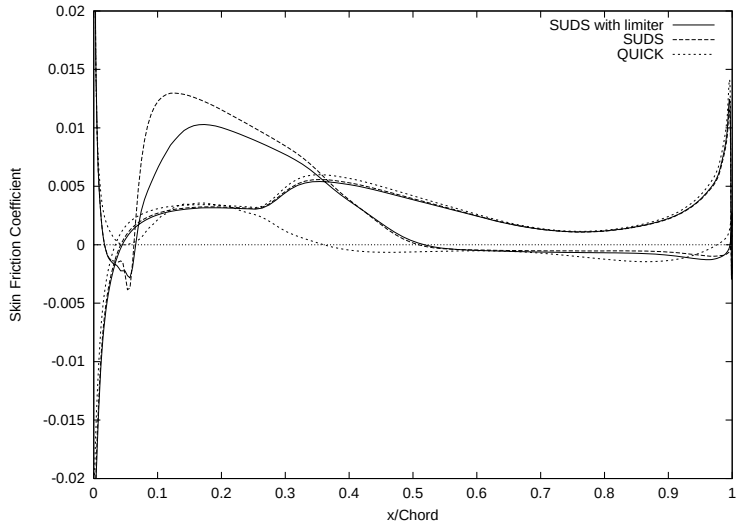

Figure 21. Skin Friction Distribution for the Different Convective Schemes at $\alpha = 15.19^o$

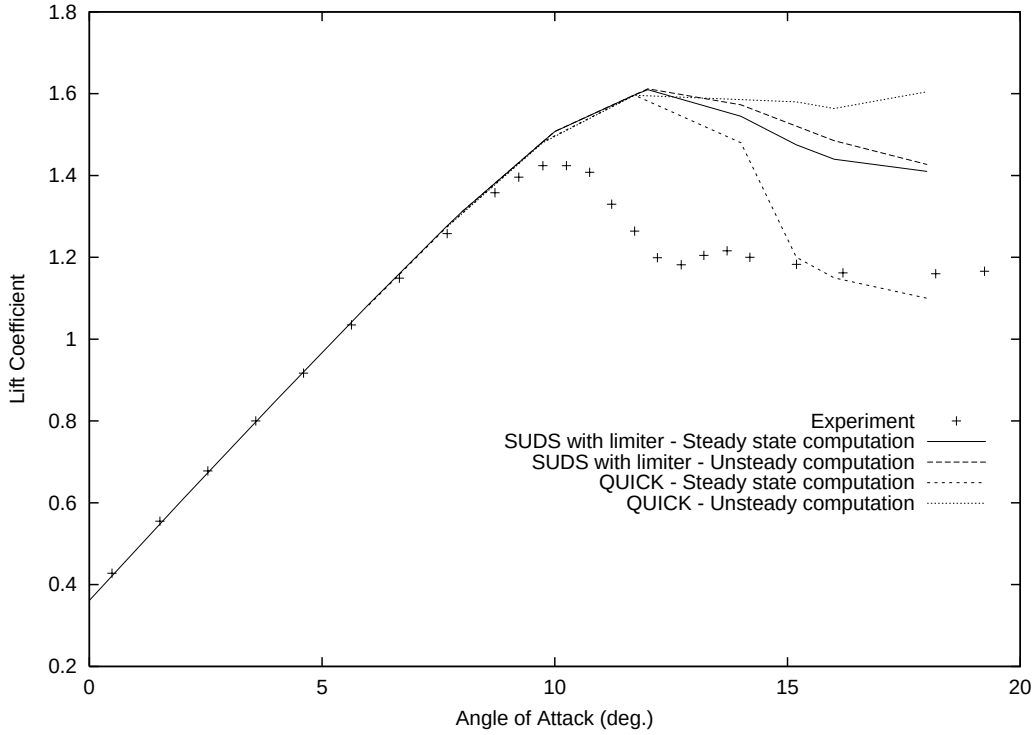

Figure 22. Lift Coefficient Curves for Steady State and Unsteady Computations

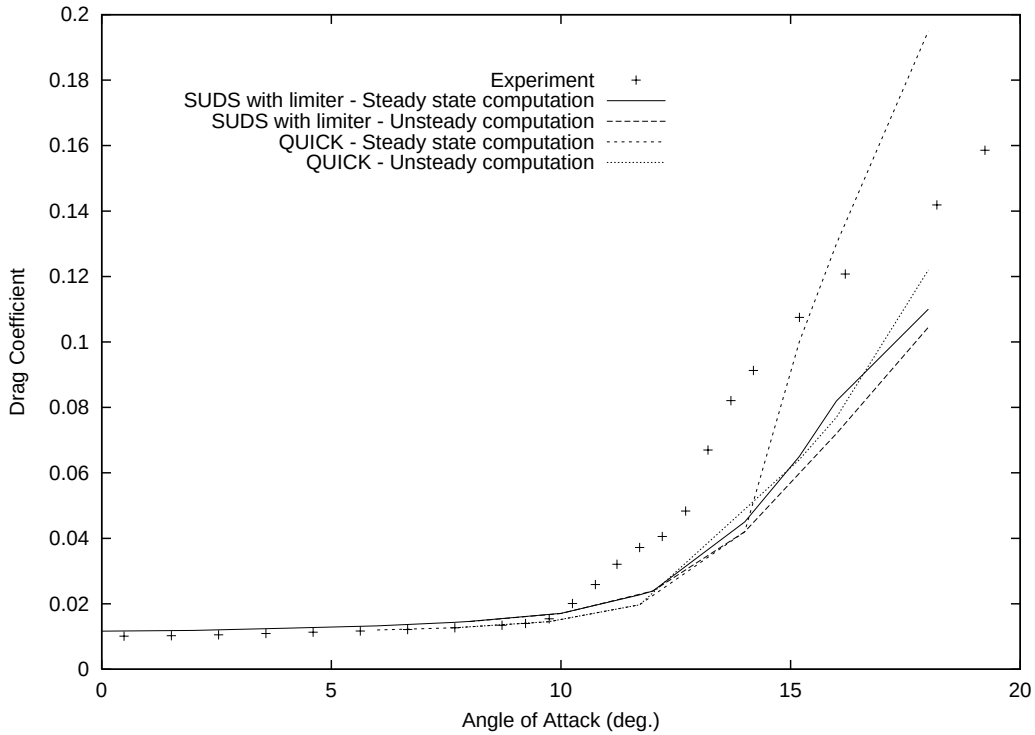

Figure 23. Drag Coefficient Curves for Steady State and Unsteady Computations

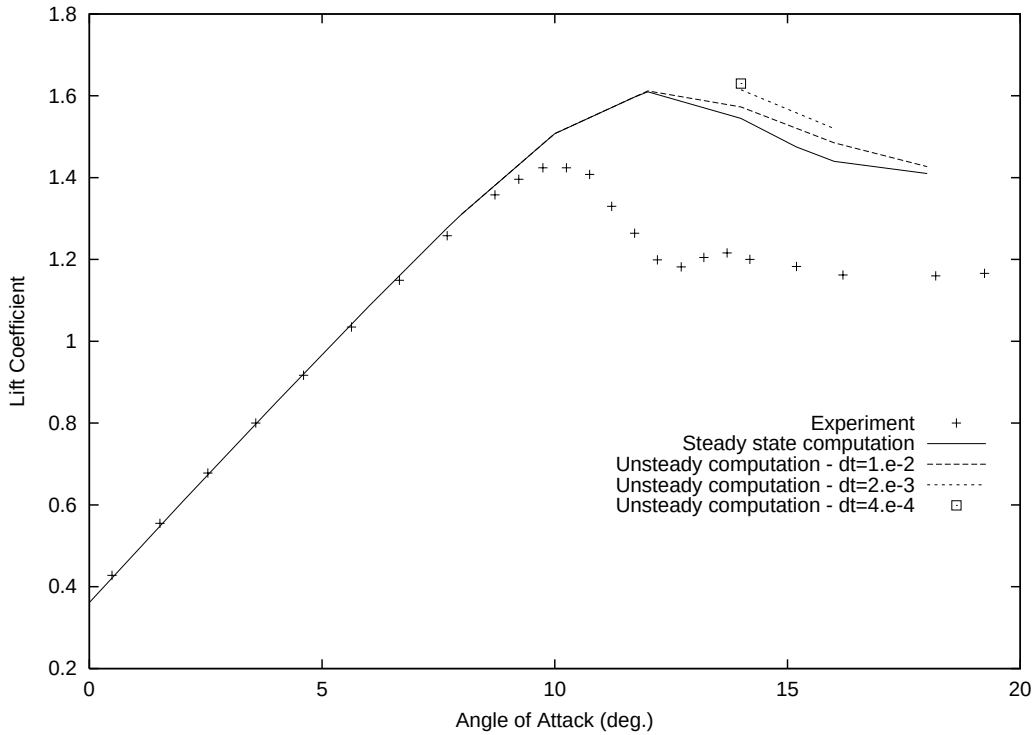

Figure 24. Lift Coefficient Curves for Different Time Steps (SUDS-scheme with limiter)

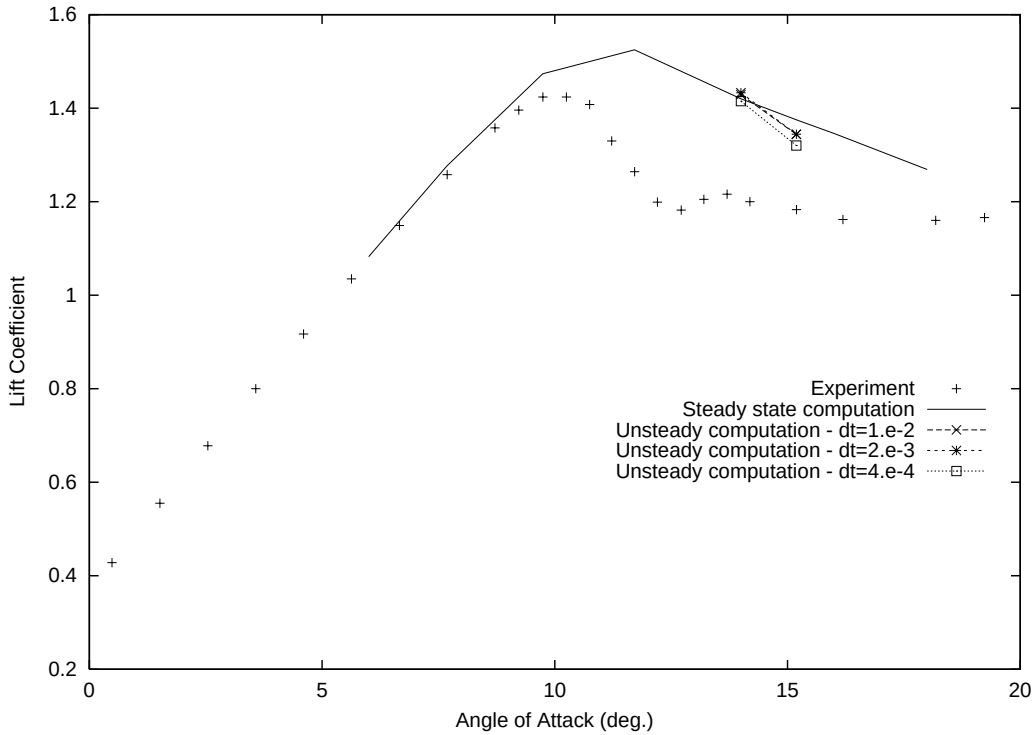

Figure 25. Lift Coefficient Curves for Different Time Steps (SUDS-scheme without limiter)

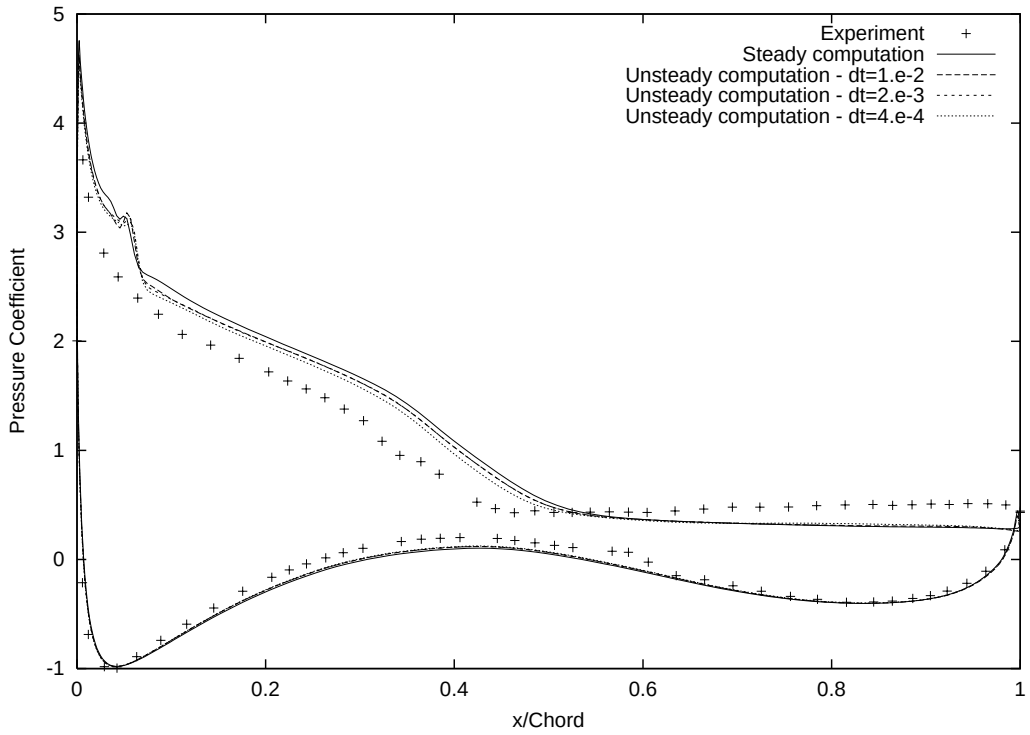

Figure 26. Pressure Distribution for Different Time Steps (SUDS-scheme without limiter, $\alpha = 15.19^o$)

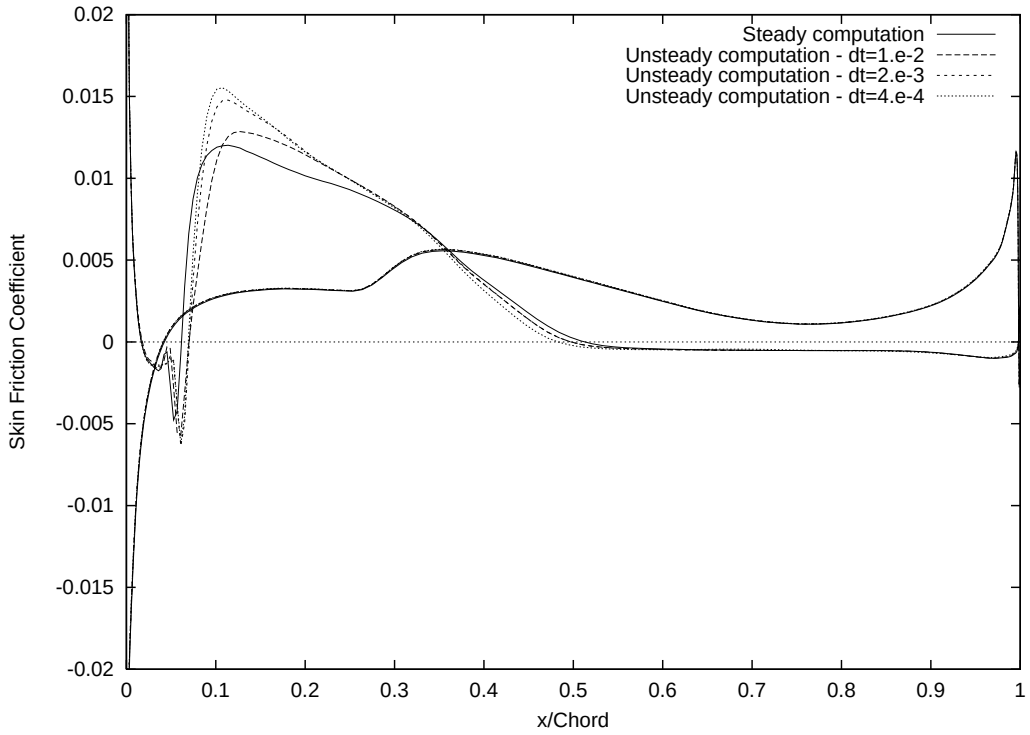

Figure 27. Skin Friction Distribution for Different Time Steps (SUDS-scheme without limiter, $\alpha = 15.19^o$)

3 A-Airfoil

The A-airfoil has been chosen as a test case for validating several numerical codes by the partners of the ECARP project, in continuation of the BRITE-EURAM/EUROVAL project [2]. It has a relative thickness of approximately 15%. Its shape is plotted on Figure 28. This airfoil was tested in the ONERA/FAUGA wind tunnels. Experimental measurements were compared to the numerical computations of the several partners. In this report, two different Reynolds number configurations are investigated: $Re = 2.1 \times 10^6$ and $Re = 5.25 \times 10^6$. Several Mach number configurations have been measured. Only measurements performed at the lowest Mach number, namely $Ma = 0.15$, are considered hereafter, so that the flow can be considered as incompressible.

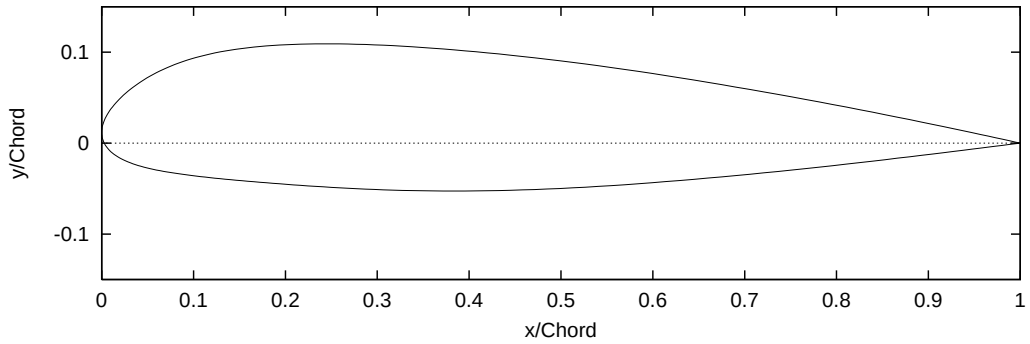

Figure 28. Shape of the A-Airfoil

The study starts with the influence of the mesh refinement, then of the convective scheme. Differences between steady and unsteady computations are investigated. Finally, the present computational results are compared with the experimental data and computations from other numerical codes.

All computations are performed with the $k - \omega$ SST turbulence model by Menter [7] and the transition model by Michel [8], as previously described in section 2.3. As the trailing edge of the airfoil profile is sharp, only C-type meshes have been used in this section. The length of the domain upstream from and on the sides of the airfoil is approximately 15 chords, whereas the mesh extends within 12 chords in the wake of the airfoil. The chord is denoted by C hereafter.

3.1 Influence of the mesh

The influence of the mesh refinement is investigated first. Three meshes are considered. The coarsest mesh, denoted as M1, contains 384 cells in the direction around the airfoil, 128 of them being in the wake, which means that there are 256 cells along the surface of the airfoil. It has 64 cells in the direction away from the airfoil, the height of the first cell next to the airfoil being equal to 1.10^{-5}. The two other meshes M2 and M3 are merely obtained by successively doubling, respectively tripling, the number of cells of mesh M1 in each direction. Consequently, mesh M2 contains 768×128 cells, which are twice as fine in each direction as the ones of mesh M1. Mesh M3 contains 1152×192 cells, three times as fine as the ones of mesh M1.

The lift and drag coefficients versus the angle of attack are compared to the experimental data obtained in the wind tunnel on Figs.29 and 30, respectively, for the SUDS-scheme, and Figs.31 and 32 for the QUICK-scheme. As it can be seen,

the finer the mesh, the higher is the angle of attack for which the airfoil starts to stall. This is true for both schemes. However, as depicted on these figures, the experiment shows an earlier stall than for all of the meshes and schemes considered.

For the coarsest mesh M1, the SUDS-scheme exhibits a smooth stall. But, for the mesh M2, an abrupt stall takes place. As for the QUICK-scheme, an abrupt stall occurs for all meshes. Moreover, when the stall has started, its level remains similar for all these meshes. However, for the finer mesh, a behaviour similar to the experiment occurs: after entering a deep stall for an angle of attack $\alpha = 20.1^o$, the airfoil recovers a moderate stall with higher lift when the angle of attack increases again (Fig.32).

Although the computations seems not to be converged with respect to the mesh refinement, the subsequent computations will be performed with the mesh M2, as the computations with mesh M3 are too expensive in terms of computational ressources.

3.2 Influence of the convective scheme

The influence of the convective scheme is now considered. The mesh M2 introduced in the previous section is used for all computations. Only the SUDS and the QUICK-scheme are investigated. Results obtained with both schemes are compared with experimental data that are available.

First, Figs.33 and 34 display the lift and drag coefficient curves. It can be seen that, in comparison with the SUDS-scheme, the QUICK-scheme predicts the stall of the airfoil for a smaller angle of attack. This is closer to the experiment, which predicts an even earlier stall. However, both schemes predict a much greater loss of lift during stall than the experiment itself. The drag coefficient computed by both schemes is slightly underestimated compared to the experimental data in the linear region. This coefficient was not experimentally measured in the stalled region.

A closer insight can be gained by looking at the pressure and skin friction coefficients along the airfoil for various angles of attack. Let us first consider an angle of attack in the linear region. The pressure and skin friction coefficients for an angle of attack $\alpha = 13.1^o$ are reported on Figs.35 and 40. Both schemes exhibit a good agreement with the experimental data.

The angle of attack $\alpha = 16.1^o$ is considered next. In the experiment, the airfoil undergoes a stall (see Fig.33), which is characterized by a larger detachment originating at the trailing edge (Fig.41) than the one observed in the linear region, thereby inducing a loss of lift due to the drop of the pressure on the suction side of the airfoil (Fig.36). The SUDS and QUICK-schemes predict that the airfoil hasn't yet entered the stalled region. However, they both give similar results.

For $\alpha = 17.1^o$, the experimental trailing edge detachment length is getting smaller again, and a higher lift is recovered (Fig.42). Both numerical schemes predict a detachement zone that has roughly the same length as the experimental one, although the amplitude of the skin friction is smaller in this region. Nevertheless, the results, including the pressure coefficient (Fig.36), are in good agreement for this angle of attack.

For $\alpha = 18.1^o$, as previously, the same conclusions can be drawn for the experimental data and the SUDS-scheme (Figs.38 and 43). In contrast, the QUICK-scheme predicts an almost fully detached flow (Fig.43), explaining the stall observed at this angle on Fig.33.

Finally, for $\alpha = 20.1^o$, the experiment and both numerical schemes predict a fully detached flow (Fig.44). However, some discrepancies can be observed. First, the experimental detachment point is observed at a station (approximately $x/C = 0.25$) located downstream of the detachment point predicted by the computations

($x/C = 0.03$). Thus, the pressure coefficient distributions along the suction side have quite different shapes, whereas both numerical schemes agree with each other (Fig.39). This explains why the losts of lift during stall observed on Fig.33 are quite different between the experiment and the computations.

3.3 Comparison between steady and unsteady simulations

In this section, some unsteady simulations are performed. Two time steps are used: $\Delta t = 1 \times 10^{-2}$ and $\Delta t = 2 \times 10^{-3}$. Mesh M2 and the SUDS-scheme have been used for these simulations.

On Figs.45 and 46, the averaged pressure and skin friction coefficients for an angle of attack $\alpha = 13.3^o$ are reported respectively, together with the results of the steady state computation. The pressure coefficient is insensitive to the time stepping procedure, whereas the skin friction coefficient indicates that, firstly, both unsteady simulations give similar results, and secondly, that the recirculation bubble induced by the transition on the suction side is a bit more intense for these unsteady computations than for the steady state computation.

3.4 Comparison with other computational codes

In this section, the computational results of the present code are compared to the results obtained with other computational codes. These latter codes were evaluated against each other in the course of the ECARP project [2]. As mentioned earlier, the experimental measurements were performed by ONERA as a part of this project. Two wind tunnels were used: F1 is more accurate but does not give access to the velocity profiles, whereas these are available in F2 which is a bit less accurate.

The purpose of these comparisons is mainly to evaluate the influence of the turbulence model. Therefore, only two of these computational codes are reported in this report. The first one is a code developed at CERFACS. It uses an algebraic stress model, which has proven to give the best agreement with the experiments over the range of incidences considered. The second one is a code from NLR with the Baldwin-Lomax / Goldberg backflow model, which shows good agreement with experimental data at low angles of attack. Both codes use an explicit Runge-Kutta temporal scheme and a finite volume discretisation with artificial dissipation. However, the code from CERFACS has a cell centered grid arrangement, whereas the NLR code has a cell vectex arrangement.

The results are compared for two configurations. The first case is for a Reynolds number equal to $Re = 2.1 \times 10^6$, at an angle of attack of $\alpha = 13.3^o$. The second case is for a Reynolds number of 5.25×10^6 at an angle of attack of $\alpha = 15.1^o$. No experimental measurements of the velocity and of the displacement and momentum thickness were performed for this last case. These two cases are located in the linear region before the airfoil has entered the stall region.

- **Case** $Re = 2.1 \times 10^6$, $\alpha = 13.3^o$

First, the lift and drag coefficients obtained for this configuration are displayed in Table 1. The present code predicts a higher lift coefficient in comparison with the other numerical codes, and a lower drag coefficient. In this table, the results of both wind tunnels F1 and F2 are reported. The tunnel F1 is considered to be more accurate than F2. In this respect, the lift coefficient shows that the present code is performing as good as the other codes, although the drag coefficient is

underpredicted.

	$Re = 2.1.10^6$, $\alpha = 13.3^o$		$Re = 5.25.10^6$, $\alpha = 15.1^o$	
	Lift Coefficient	Drag Coefficient	Lift Coefficient	Drag Coefficient
Experiment (F1)	1.56	0.0204	1.72	0.0241
Experiment (F2)	1.52	0.0308	-	-
Present	1.59	0.0175	1.80	0.0161
CERFACS	1.53	0.0208	1.80	0.0193
NLR	1.52	0.0185	1.82	0.0209

Table 1. Comparison of Force Coefficients for the Different Numerical Codes

The pressure and skin friction coefficients are considered next. Their values on the airfoil surface are reported on Figs.47 and 48, respectively. The skin friction coefficient is displayed only on the suction side. When the pressure coefficients are in good agreement for all computational codes, the skin friction coefficients present some discrepancies. An important point is that the present code predicts a very small detached region at the trailing edge, whereas the two other codes predict a larger one, in accordance with the experiment. Furthermore, the present code predicts a laminar separation bubble located approximately at the station $x/C = 0.15$, which is not captured by the other numerical codes. Although the measurements of the skin friction coefficient are not provided in this specific area, the existence of this bubble is mentioned in the ECARP-report [2]. These facts might also suggest that the transition point of the present computation, which is located more downstream on the suction side than for the two other codes (see Fig.48), should be enforced at an upstream location in order to recover the correct behaviour.

The displacement and momentum thickness along the suction side of the airfoil are displayed on Figs.49 and 50. Again, some discrepancies exist between the different codes. However, it turns out that the Baldwin-Lomax turbulence model with Goldberg backflow model from NLR produces the results the closest to the experiment. The CERFACS code tends to overpredict the thickness of the boundary layer, whereas the present code tends to underpredict it.

Finally, the velocity profiles at several stations near the trailing edge (Figs.51,52, 53) and in the near wake of the airfoil (Figs.54,55) are displayed. As expected, the profiles near the trailing edge show that the detachment is hardly captured by the present method. However, it performs normally in the near wake.

• **Case** $Re = 5.25 \times 10^6$, $\alpha = 15.1^o$

The lift and drag coefficients are displayed on Table 1. The present code predicts the same lift as the CERFACS code, whereas the NLR code gives a higher lift. All of the computational results are above the experimental value (Note that only tunnel F2 has been used for this configuration). The computed drags are all below the experimental value. The NLR code gives the closest result, and the present code largely underestimates this value.

The pressure and skin friction coefficients and displacement thickness curves on the airfoil are presented on Figs.56,57 and 58, respectively. The same conclusions as for the previous case can be drawn.

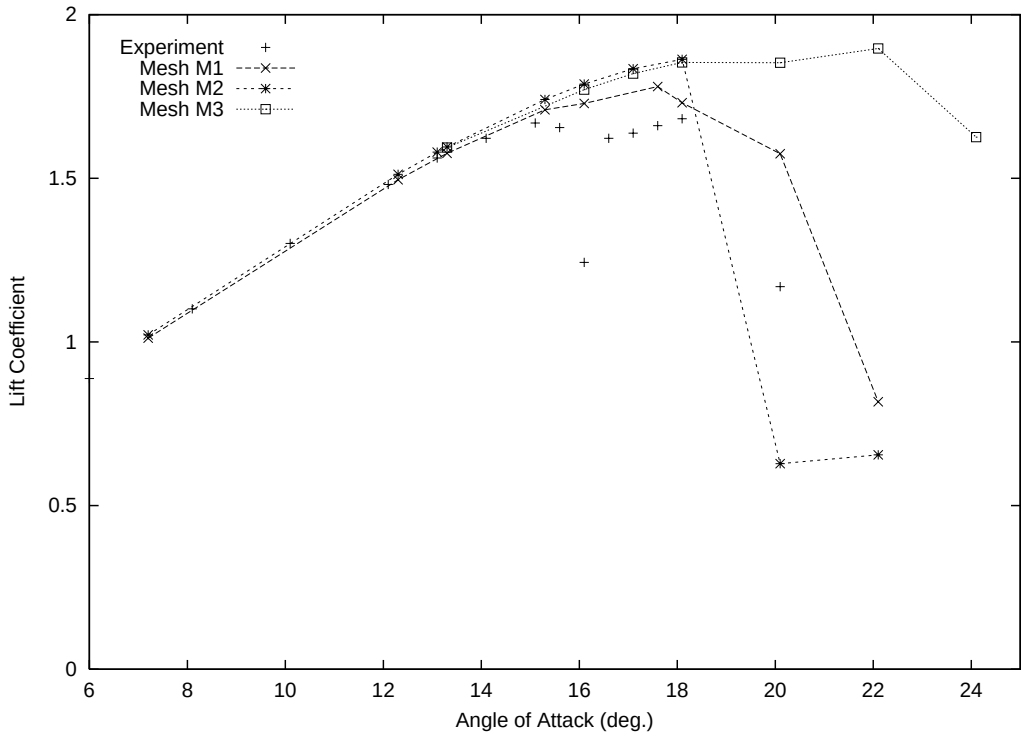

Figure 29. Lift Coefficient Curves for the Different Meshes with the SUDS-Scheme

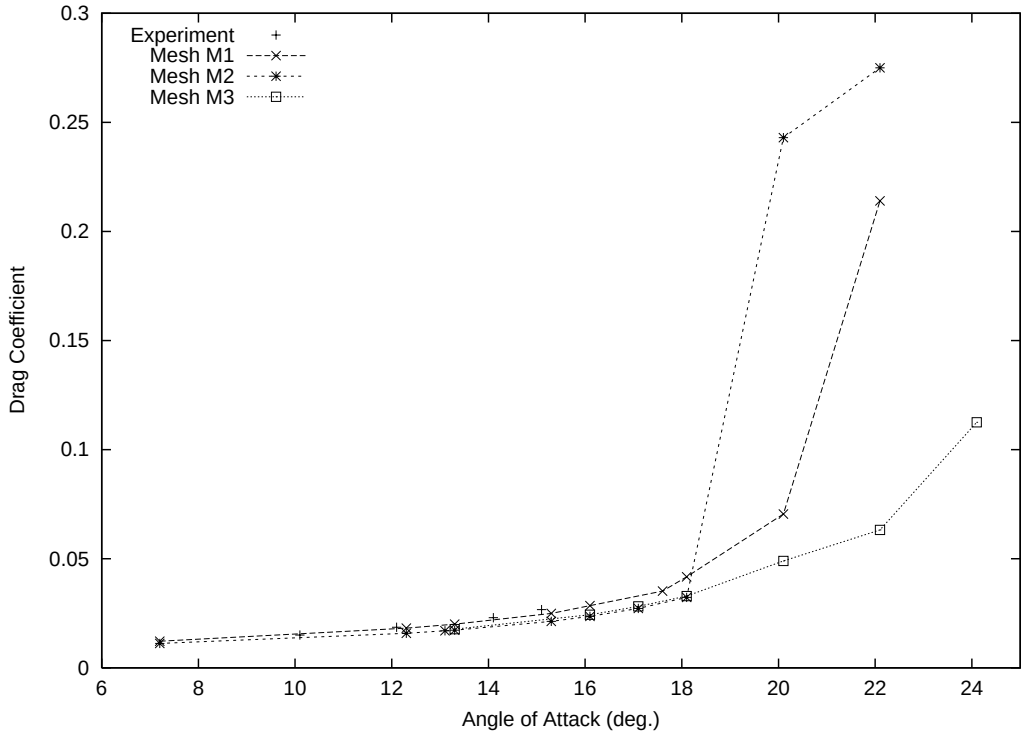

Figure 30. Drag Coefficient Curves for the Different Meshes with the SUDS-Scheme

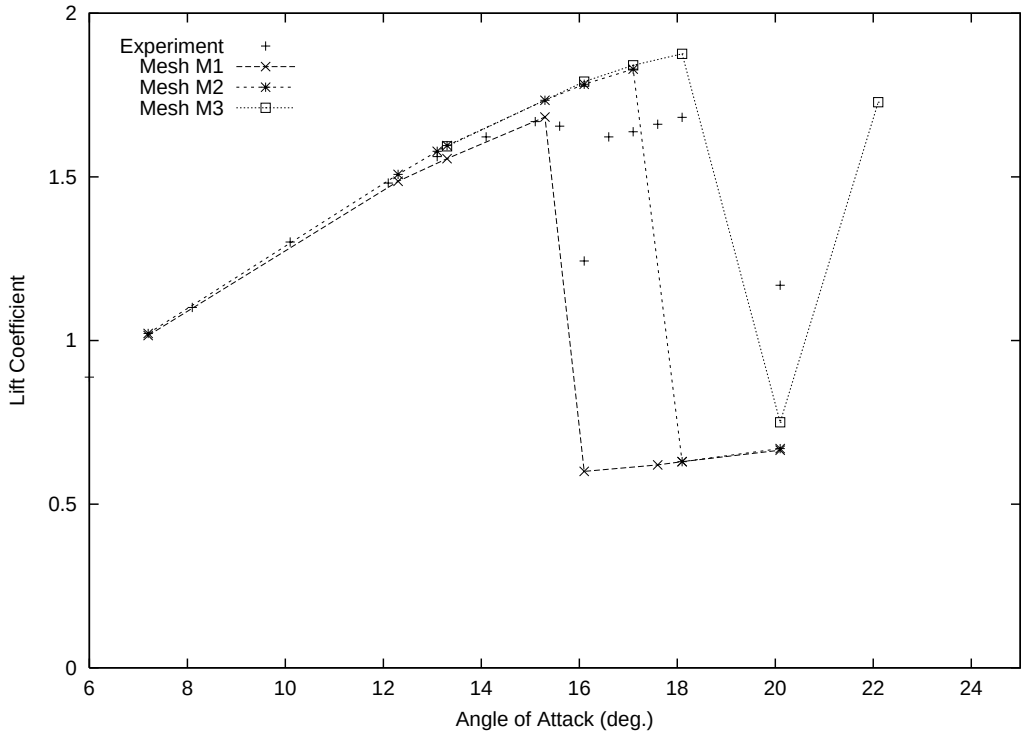

Figure 31. Lift Coefficient Curves for the Different Meshes with the QUICK-Scheme

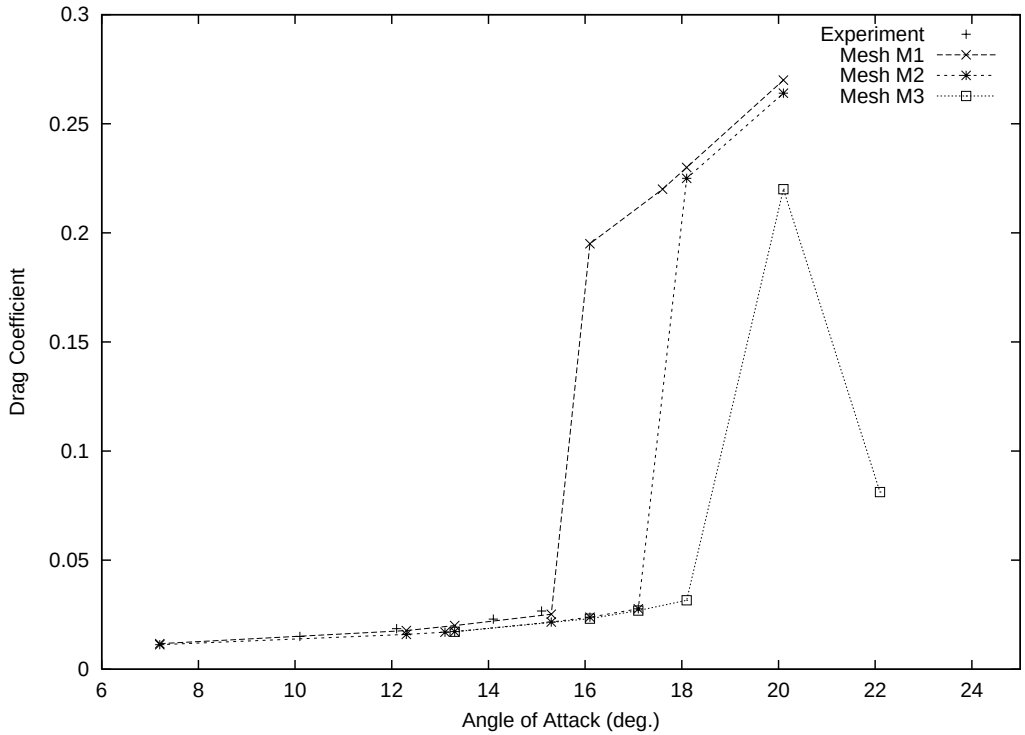

Figure 32. Drag Coefficient Curves for the Different Meshes with the QUICK-Scheme

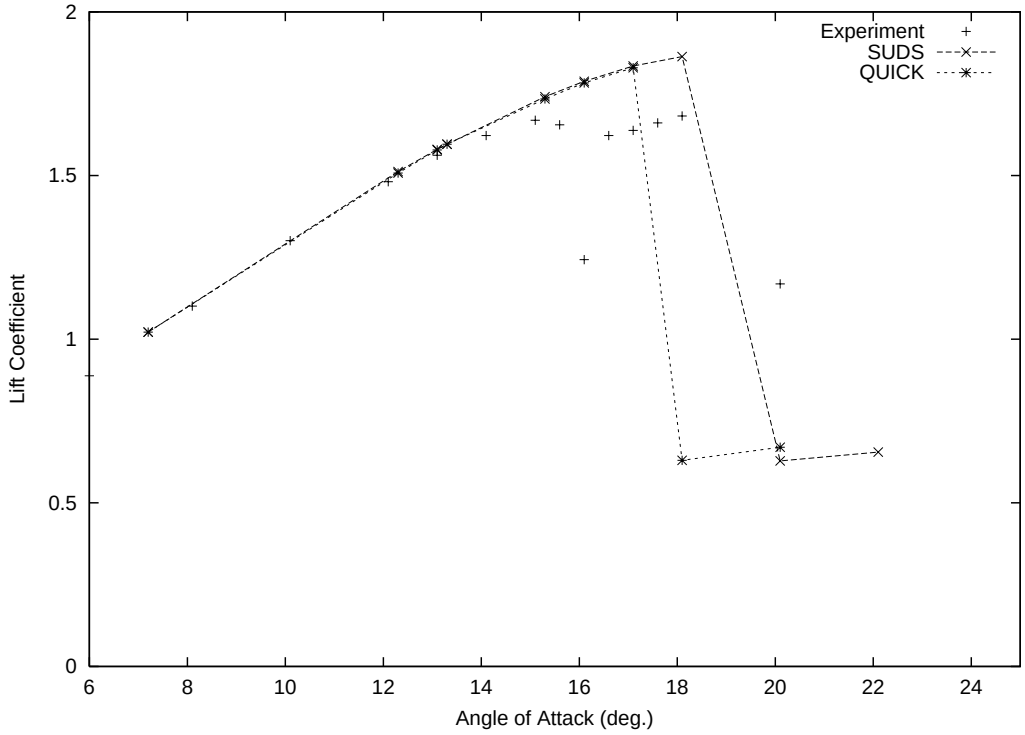

Figure 33. Lift Coefficient Curves for the Different Convective Schemes

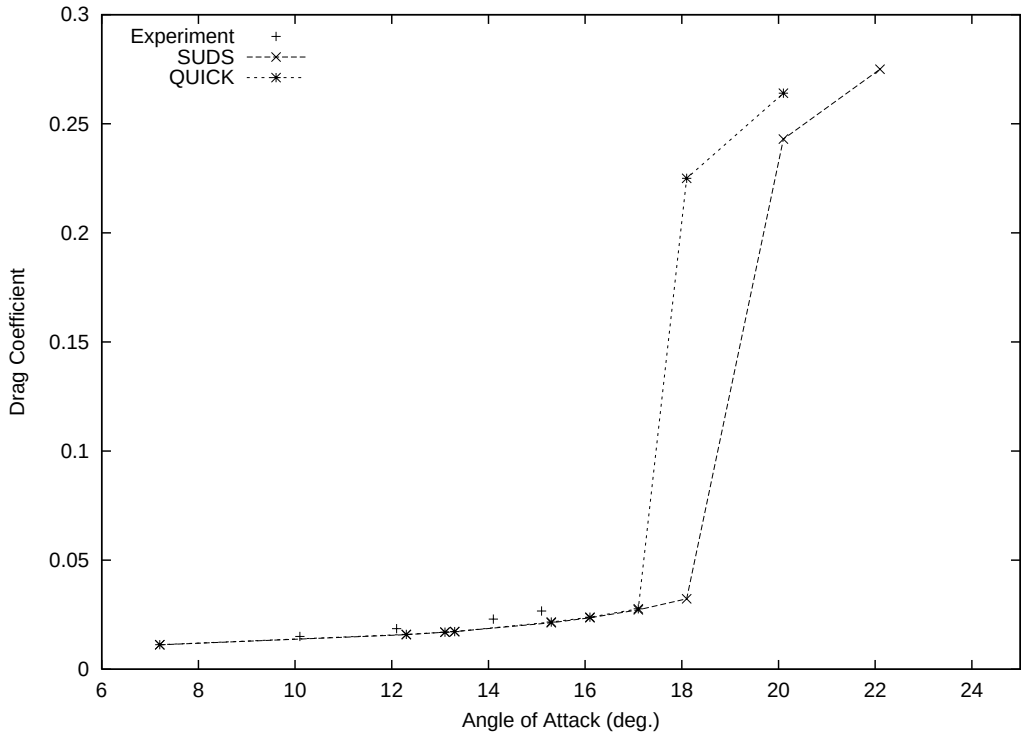

Figure 34. Drag Coefficient Curves for the Different Convective Schemes

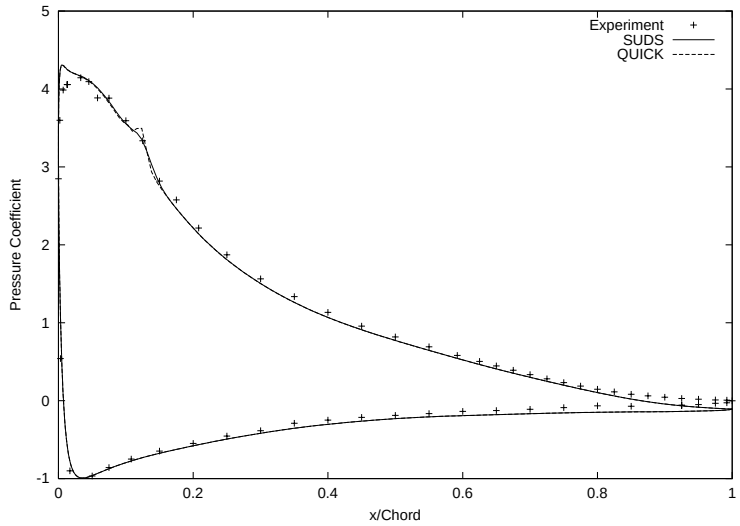

Figure 35. Pressure Distribution for the Different Convective Schemes at $\alpha = 13.1^o$

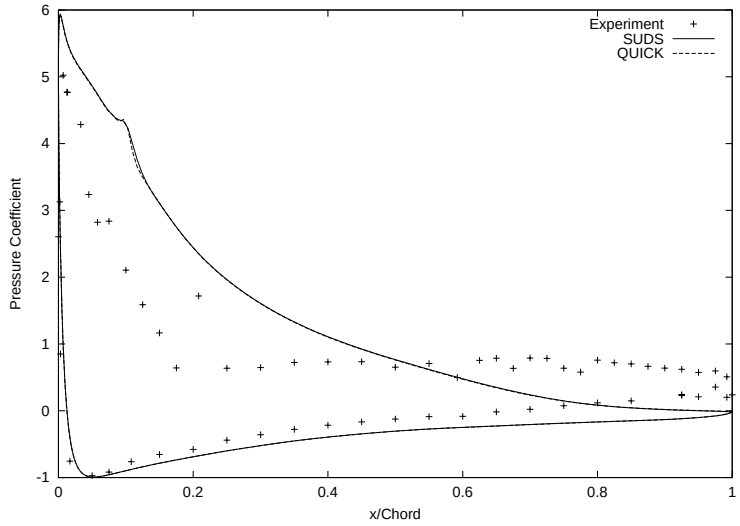

Figure 36. Pressure Distribution for the Different Convective Schemes at $\alpha = 16.1^o$

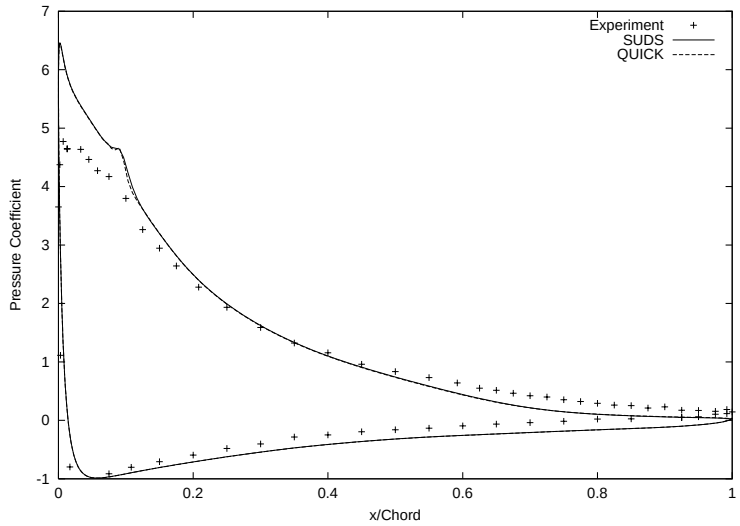

Figure 37. Pressure Distribution for the Different Convective Schemes at $\alpha = 17.1^o$

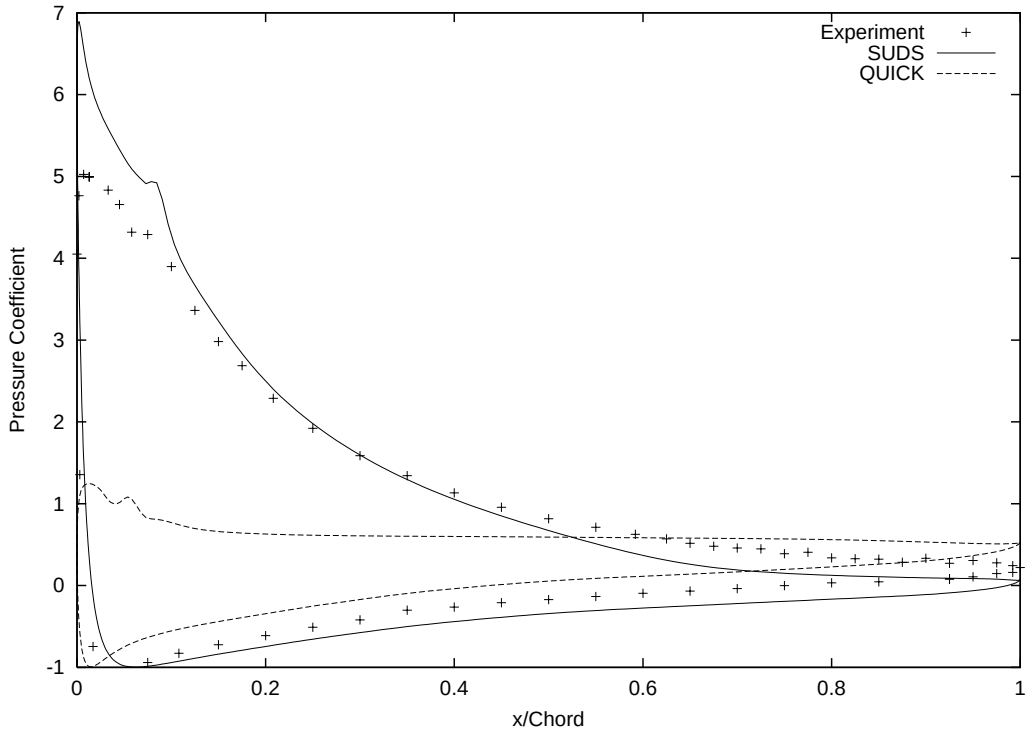

Figure 38. Pressure Distribution for the Different Convective Schemes at $\alpha = 18.1^o$

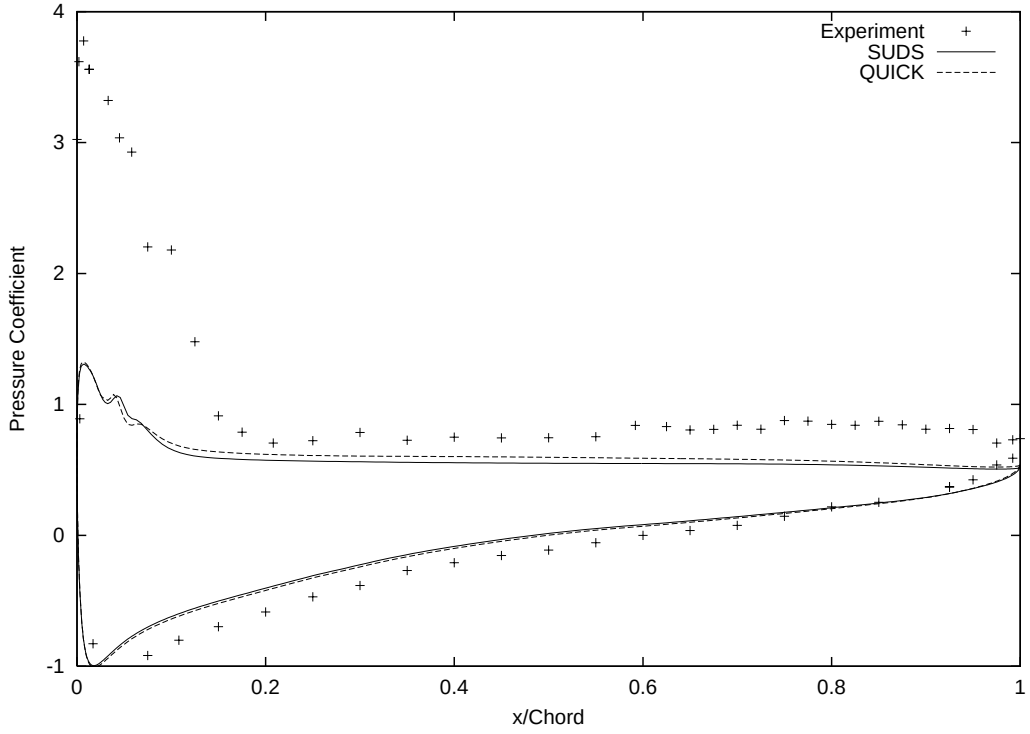

Figure 39. Pressure Distribution for the Different Convective Schemes at $\alpha = 20.1^o$

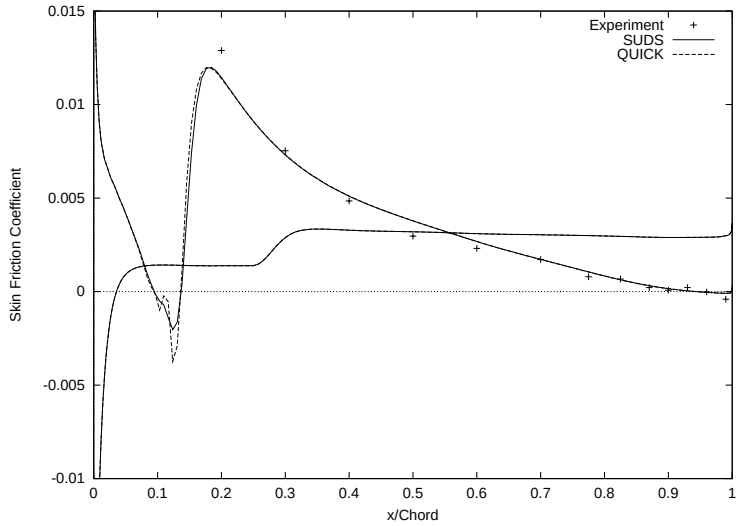

Figure 40. Skin Friction Distribution for the Different Convective Schemes at $\alpha = 13.1^o$

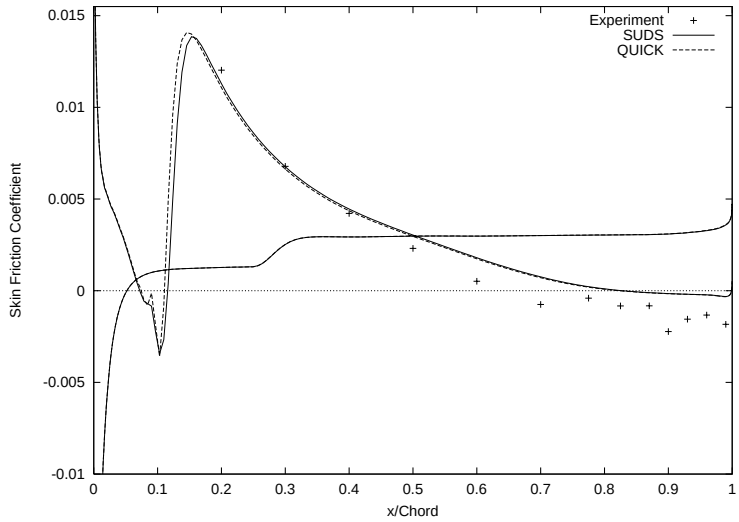

Figure 41. Skin Friction Distribution for the Different Convective Schemes at $\alpha = 16.1^o$

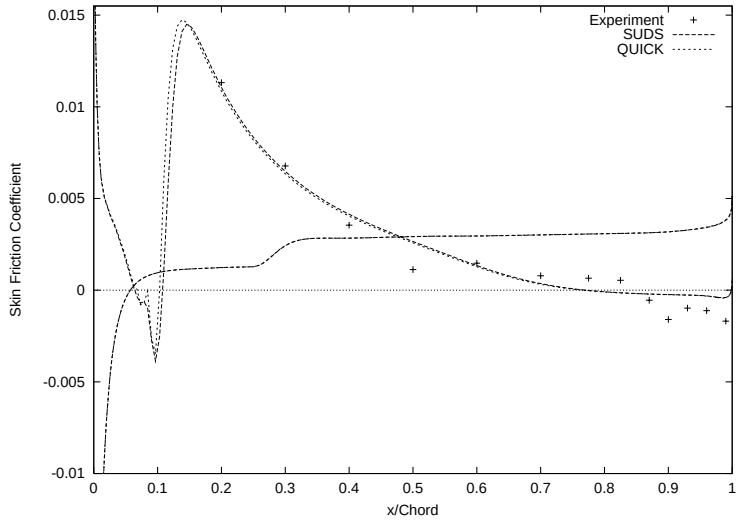

Figure 42. Skin Friction Distribution for the Different Convective Schemes at $\alpha = 17.1^o$

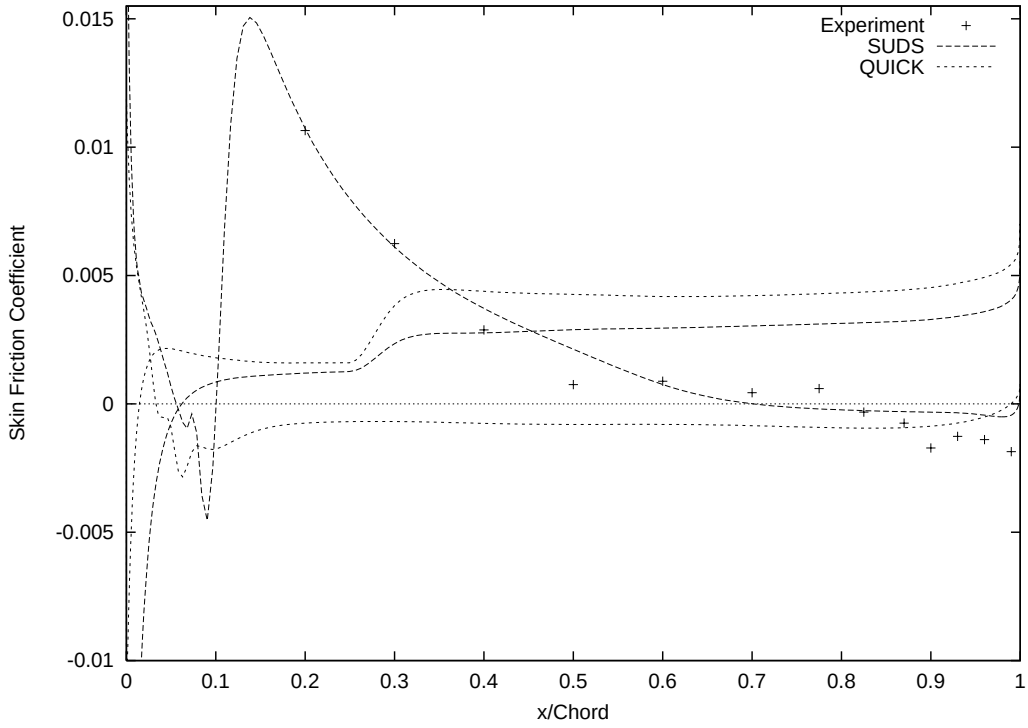

Figure 43. Skin Friction Distribution for the Different Convective Schemes at $\alpha = 18.1^o$

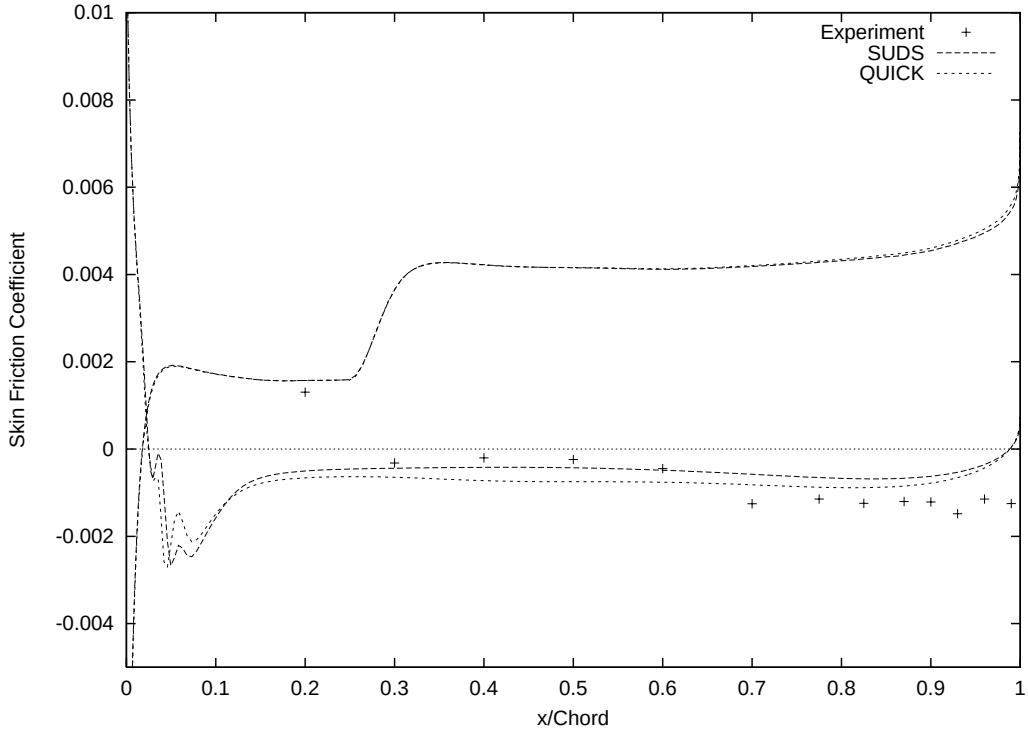

Figure 44. Skin Friction Distribution for the Different Convective Schemes at $\alpha = 20.1^o$

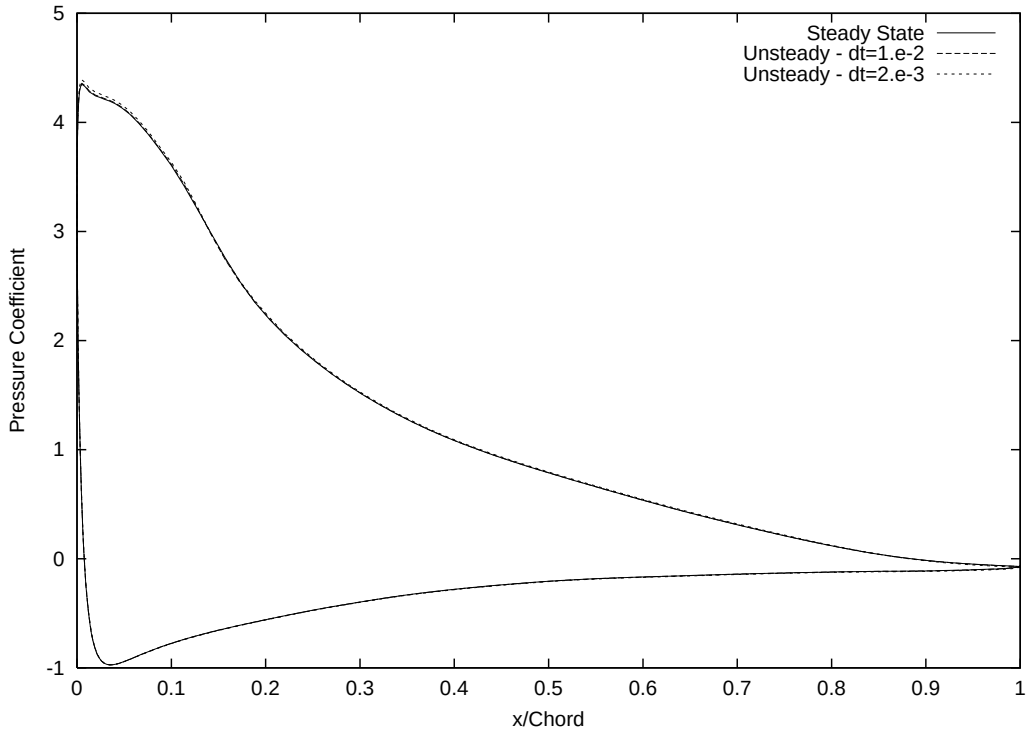

Figure 45. Pressure Distribution for the Steady State and Unsteady Computations ($\alpha = 13.3^o$)

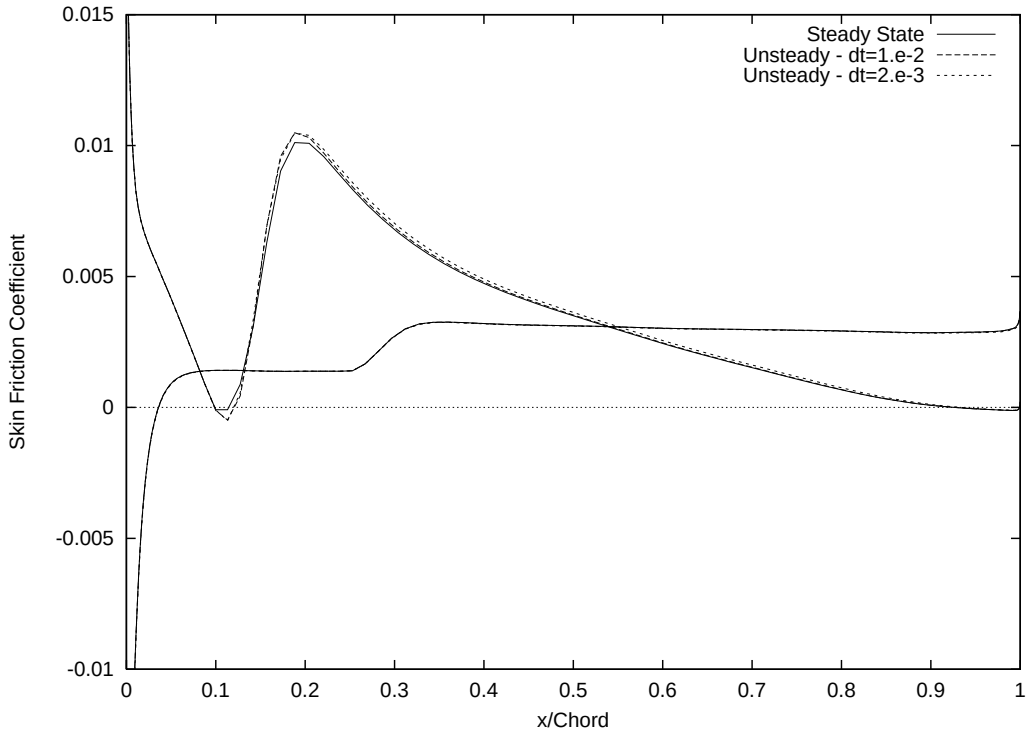

Figure 46. Skin Friction Distribution for the Steady State and Unsteady Computations ($\alpha = 13.3^o$)

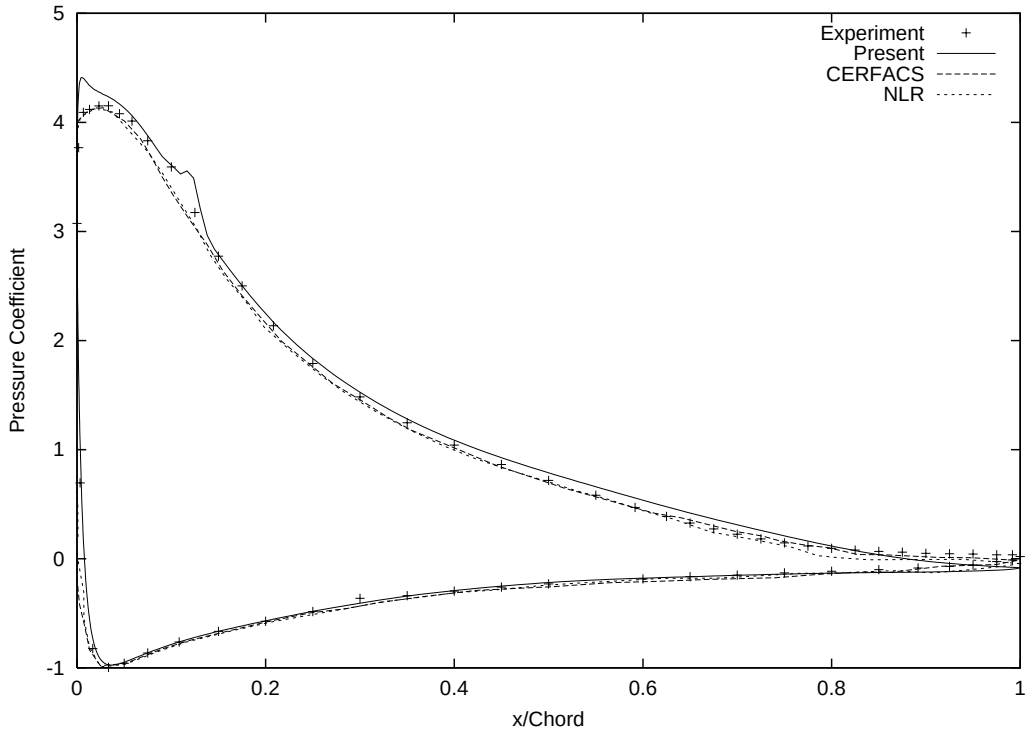

Figure 47. Pressure Distribution for the Different Numerical Codes and Experiment ($Re = 2.1 \times 10^6$, $\alpha = 13.3^o$)

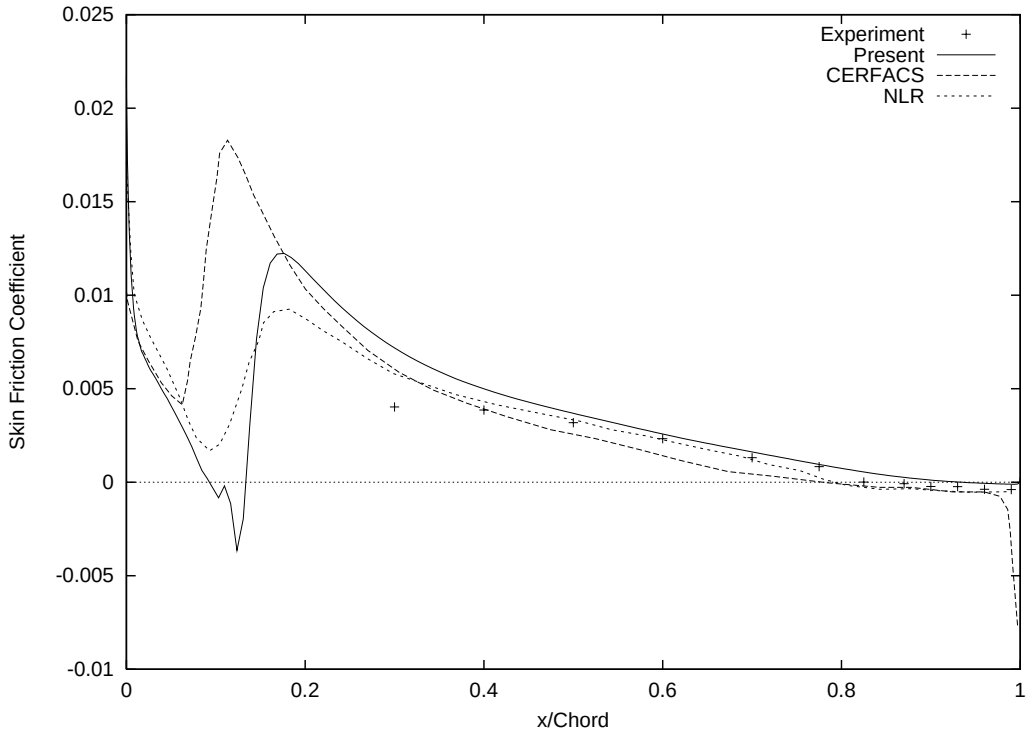

Figure 48. Skin Friction Distribution for the Different Numerical Codes and Experiment ($Re = 2.1 \times 10^6$, $\alpha = 13.3^o$)

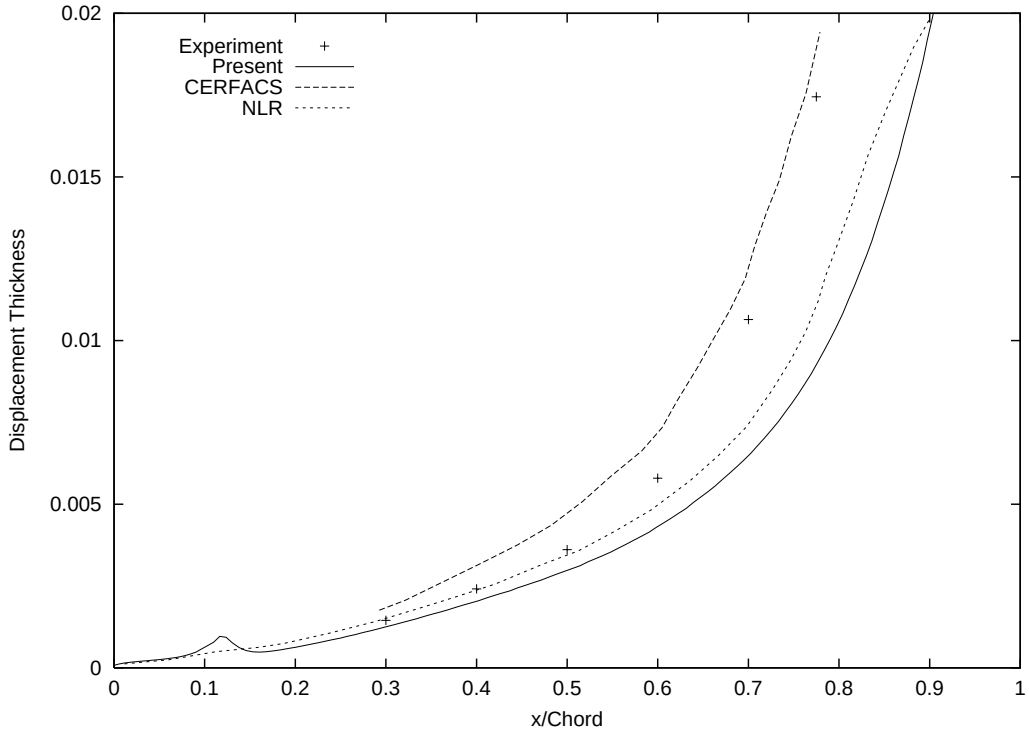

Figure 49. Displacement Thickness for the Different Numerical Codes and Experiment ($Re = 2.1 \times 10^6$, $\alpha = 13.3^o$)

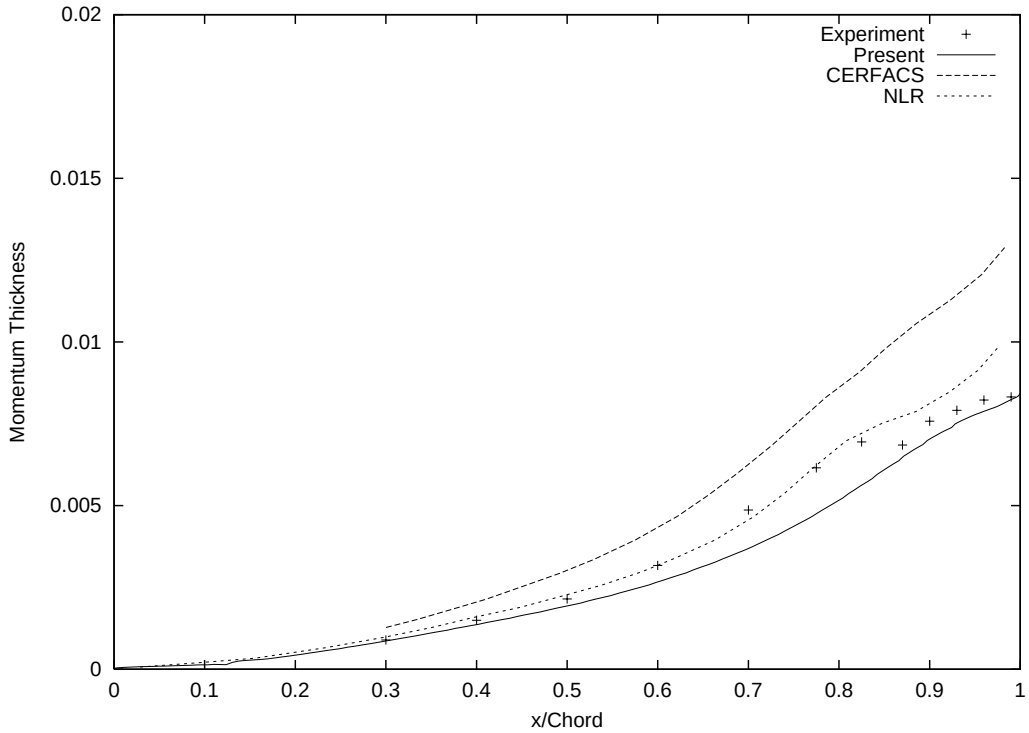

Figure 50. Momentum Thickness for the Different Numerical Codes and Experiment ($Re = 2.1 \times 10^6$, $\alpha = 13.3^o$)

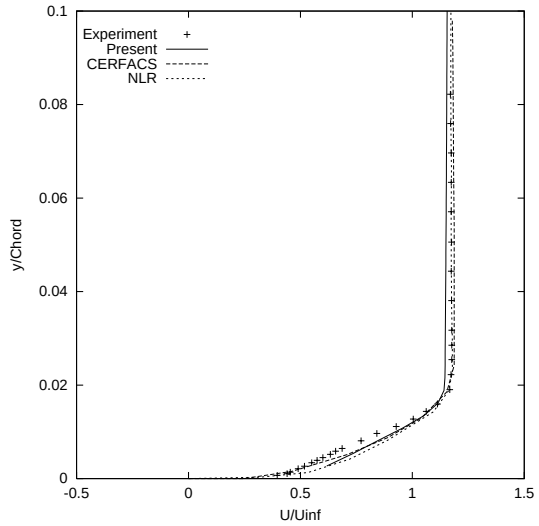

Figure 51. Velocity Profiles for the Different Numerical Codes and Experiment (Station $x/C = 0.6$, $Re = 2.1 \times 10^6$, $\alpha = 13.3^o$)

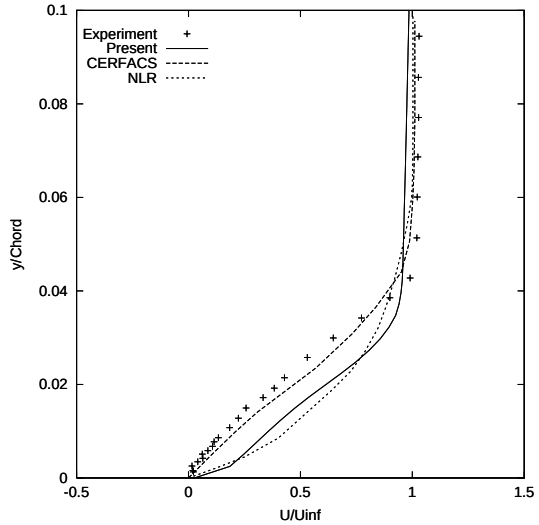

Figure 52. Velocity Profiles for the Different Numerical Codes and Experiment (Station $x/C = 0.825$, $Re = 2.1 \times 10^6$, $\alpha = 13.3^o$)

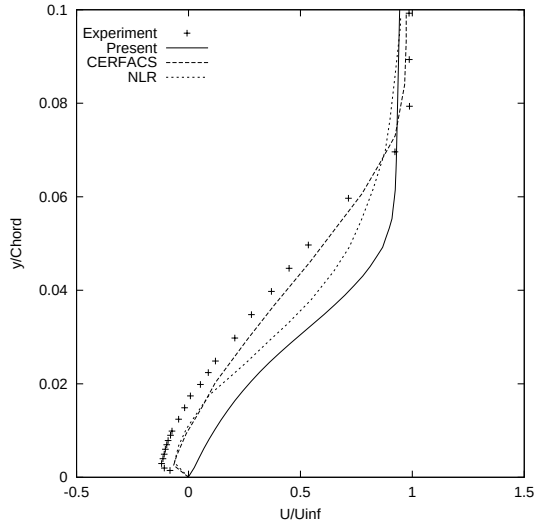

Figure 53. Velocity Profiles for the Different Numerical Codes and Experiment (Station $x/C = 0.96$, $Re = 2.1 \times 10^6$, $\alpha = 13.3^o$)

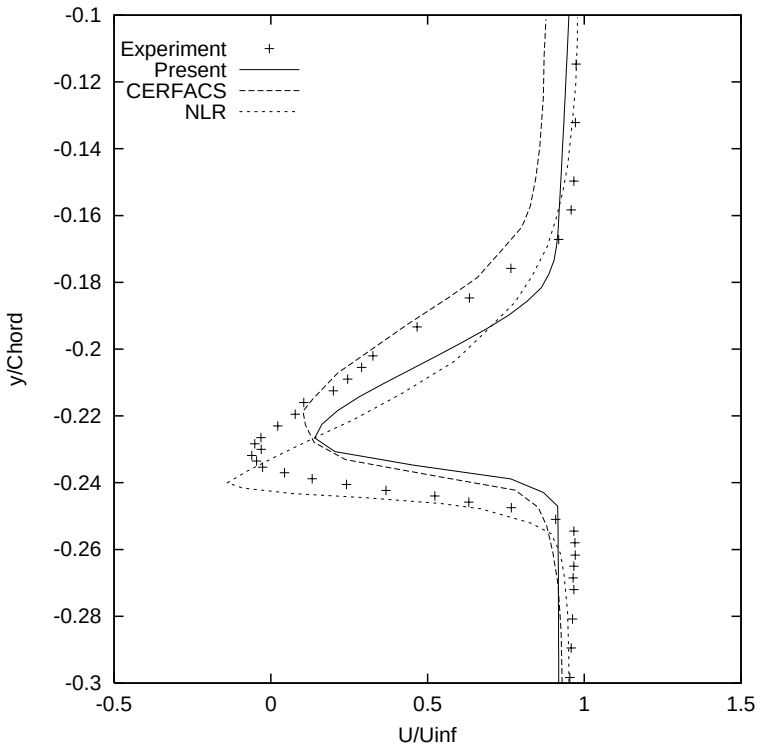

Figure 54. Velocity Profiles for the Different Numerical and Experiment (Station $x/C = 1.05$, $Re = 2.1 \times 10^6$, $\alpha = 13.3^o$*)*

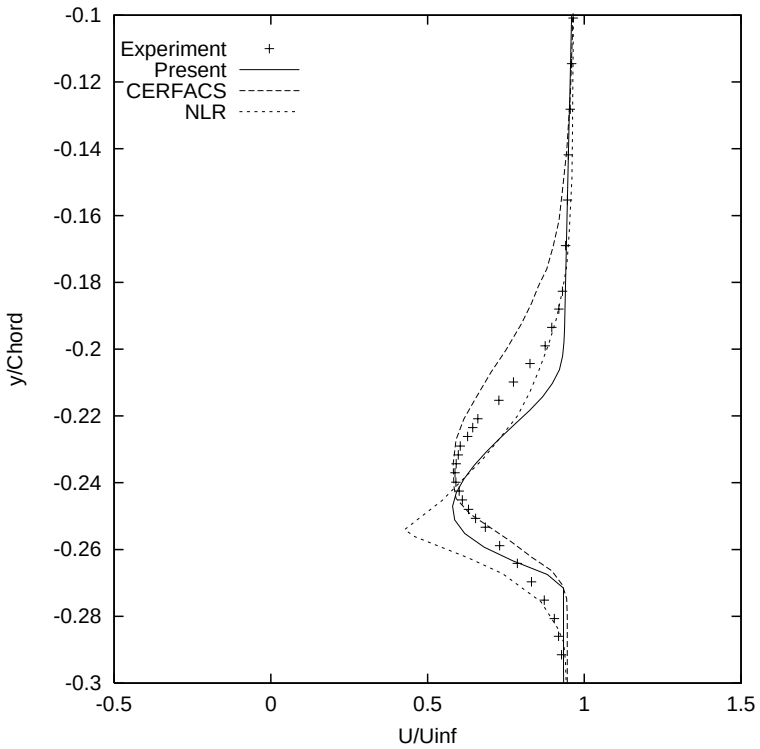

Figure 55. Velocity Profiles for the Different Numerical and Experiment (Station $x/C = 1.25$, $Re = 2.1 \times 10^6$, $\alpha = 13.3^o$*)*

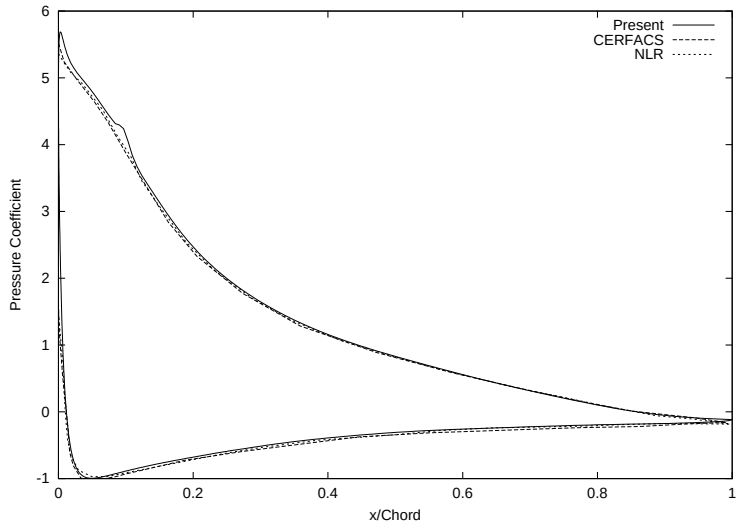

Figure 56. Pressure Distribution for the Different Numerical Codes ($Re = 5.25 \times 10^6$, $\alpha = 15.1^o$)

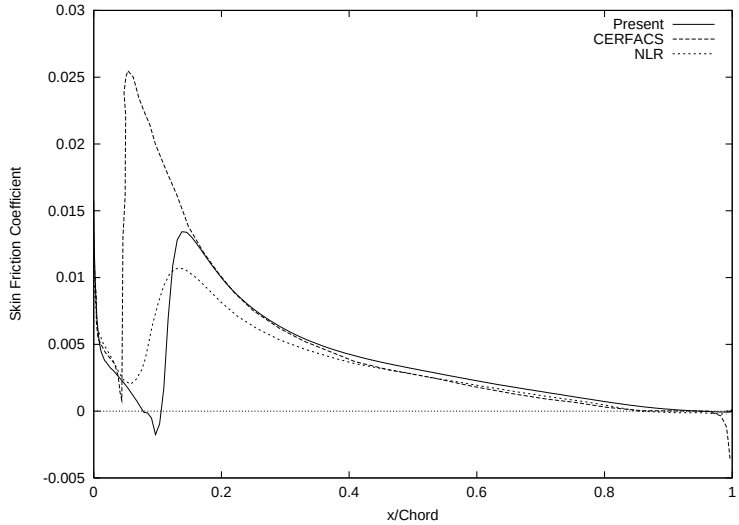

Figure 57. Skin Friction Distribution for the Different Numerical Codes ($Re = 5.25 \times 10^6$, $\alpha = 15.1^o$)

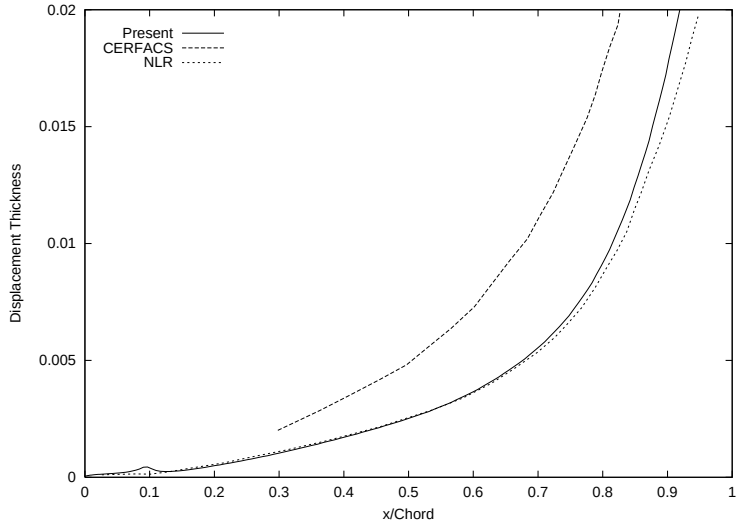

Figure 58. Displacement Thickness for the Different Numerical Codes ($Re = 5.25 \times 10^6$, $\alpha = 15.1^o$)

4 Conclusions

In this report, the behaviour of the numerical flow solver EllipSys2D has been investigated for a couple of airfoils. Simulation results were confronted to experimental data and results from other computational codes. Several general conclusions can be drawn.

An analysis of the mesh dependency on the computational results has shown that is it difficult to obtained convergence with respect to the cell mesh size. This conclusion applies only in the stall region, whereas rather coarse meshes are sufficient for the simulations within the linear region. For Reynolds numbers in the range of the million, meshes containing 64 cells in the direction away from the airfoil and 256 cells around the airfoil itself are recommended. The cell heigth at the airfoil must be of the order of 10^{-5}.

Two different convective schemes have been used: the SUDS and the QUICK-scheme. In addition, the influence of the 'min-mod' limiter have been investigated in combination with the SUDS-scheme. The SUDS and the QUICK-scheme give similar results overall. Sometimes, the QUICK-scheme seems to produce better results, but it is difficult to assess if this is due to a better apprehension of the physics of the phenomenon. However, the SUDS is slightly more stable and it is therefore to be prefered. It has been clearly shown that the use of the limiter is detrimental. It produces too much numerical dissipation and excessively increases the lift in the stalled region.

Some unsteady computations have been performed and compared to the steady state results. Whereas no differences were observed in the linear region, no particular improvement was obtained in the stalled region. A convergence study with respect to the time step was not conclusive. Thus, steady state computations are recommended. They require moreover much less computational time.

It is well-known that transition modelling is a great issue in airfoil numerical simulations. It has been here again observed that the transition model is necessary to correctly reproduce the experimental results in the linear region. In the stalled region, a fully turbulent computation give results closer to the experiment than a computation with transition model. However, it can not be concluded that it is closer to the physics of the detached flow. Indeed, it is believed that the two-dimensional computations are intrinsically unable to simulate the flow patterns that are observed in the real three-dimensional phenomenon.

As a conclusion, it can be said that the two-dimensional flow solver EllipSys2D give good results in the linear region with the help of a transition model, and fairly good results in the stalled region. However, the reasons of the discrepancies in this last case need further investigation. In particular, the location of the laminar transition in the vicinity of the trailing edge greatly influences the development of the associated laminar recirculation bubble and the subsequent trailing edge separation.

References

[1] K.K. Chen and N.A. Thyson, Extensions of Emmons Spot Theory to Flows on Blunt Bodies, *AIAA Journal*, **9**, No.5, 1971.

[2] P. Gendre, Task 2.1: Maximum Lift for Single-Element Airfoils : Experimental Results on A-Airfoil Geometry, *Brite-Euram EUROVAL*, CERFACS, France, 1992.
D.P. Hills, Aerodays '93, Conference Proceedings, Naples, 4-5 octobre 1993, pp.91-99.

[3] "ECARP – European Computational Aerodynamics Research Project: Validation of CFD codes and Assessment of Turbulence Models", *Notes on Numerical Fluid Mechanics*, edited by W. Haase, E. Chaput, E. Elsholz, M.A. Leschziner and U.R. Müller, Vol.58, Vieweg Verlag, 1997.

[4] "EUROVAL – A European Initiative on Validation of CFD-Codes", *Notes on Numerical Fluid Mechanics*, edited by W. Haase, F. Brandsma, E. Elsholz, M. Leschziner and D. Schwamborn, Vol.42, Vieweg Verlag, 1993.

[5] H.T. Huynh, Second Order Accurate Non-Oscillatory Schemes for Scalar Conservation Laws, Tech. Report, NASA TM 102010, 1989.

[6] B.P. Leonard, A Stable and Accurate Convective Modelling Procedure Based on Quadratic Upstream Interpolation, *Comp. Meth. Appl. Mech. Eng.*, **19**, 1979.

[7] F.R. Menter, Zonal Two-Equations $k-\omega$ Turbulence Models for Aerodynamic Flows, *AIAA Paper 93-2906*, 1993.

[8] R. Michel, Etude de la transition sur les profils d'aile ; Etablissement d'un critère de détermination du point de transition et calcul de la trainée de profil incompressible, Tech. Report, ONERA, Report 1/1578A, 1951.

[9] J.A. Michelsen, Basis3D - A Platform for Development of Multiblock PDE Solvers, Tech. Report, Technical University of Denmark, AFM 92-05, 1992.

[10] J.A. Michelsen, Block Structured Multigrid Solution of 2D and 3D Elliptic PDE's, Tech. Report, Technical University of Denmark, AFM 94-06, 1994.

[11] S.V. Patankar and D.B. Spalding, A Calculation Procedure for Heat, Mass and Momentum Transfer in Three-Dimensional Parabolic Flows, *Int. J. Heat Mass Transfer*, **15**, p.1787, 1972.

[12] C.M. Rhie and W.L. Chow, Numerical Study of the Turbulent Flow Past an Airfoil with Trailing Edge Separation, *AIAA Journal*, **21**, pp.1525-1532, 1983.

[13] N.N. Sørensen, General Purpose Flow Solver Applied to Flow over Hills, Tech. Report, Risø National Laboratory, Roskilde, Denmark, PhD Thesis, Risø-R-827(EN), June 1995.

[14] N.N. Sørensen, HypGrid2D - a 2D Mesh Generator, Tech. Report, Risø National Laboratory, Roskilde, Denmark, Risø-R-1035(EN), March 1998.

[15] W.A. Timmer and R.P.J.O.M. van Rooy, Wind Tunnel Results for a 25% Thick Wind Turbine Blade Airfoil, *European Community Wind Energy Conference*, 8-12 march, 1993, Lübeck-Travemünde, Germany.

[16] R.W. Yeo, P.E. Wood and A.N. Hrymak, A Numerical Study of Laminar 90-degree Bend Duct Flow with Different Discretization Schemes, *J. Fluids Eng.*, **113**, 1991.

Bibliographic Data Sheet **Risø–R–1282(EN)**

Title and author(s)

Status for the Two-Dimensional Navier-Stokes Solver EllipSys2D

Franck Bertagnolio, Niels Sørensen and Jeppe Johansen

ISBN
87–550–2914–0
87–550–2915–9(Internet)

ISSN
0106–2840

Dept. or group
Aeroelastic Design
Wind Energy Department

Date
August 2001

Groups own reg. number(s)

Project/contract No.

Pages	Tables	Illustrations	References
40	1	58	16

Abstract (Max. 2000 char.)

This report sets up an evaluation of the two-dimensional Navier-Stokes solver EllipSys2D in its present state. This code is used for blade aerodynamics simulations in the Aeroelastic Design group at Risø. Two airfoils are investigated by computing the flow at several angles of attack ranging from the linear to the stalled region. The computational data are compared to experimental data and numerical results from other computational codes. Several numerical aspects are studied, as mesh dependency, convective scheme, steady state versus unsteady computations, transition modelling. Some general conclusions intended to help in using this code for numerical simulations are given.

Descriptors INIS/EDB

AERODYNAMICS; AIRFOILS; COMPUTATIONAL FLUID DYNAMICS; E CODES; EVALUATION; NAVIER-STOKES EQUATIONS; TWO-DIMENSIONAL CALCULATIONS

Available on request from:
Information Service Department, Risø National Laboratory
(Afdelingen for Informationsservice, Forskningscenter Risø)
P.O. Box 49, DK–4000 Roskilde, Denmark
Phone (+45) 46 77 46 77, ext. 4004/4005 · Fax (+45) 46 77 4013